Microglial activation states drive glucose uptake and FDG-PET alterations in neurodegenerative diseases

Xianyuan Xiang[1,2], Karin Wind[3,4], Thomas Wiedemann[3], Tanja Blume[3,4], Yuan Shi[4], Nils Briel[4], Leonie Beyer[3], Gloria Biechele[3], Florian Eckenweber[3], Artem Zatcepin[3,4], Sven Lammich[1], Sara Ribicic[4], Sabina Tahirovic[4], Michael Willem[1], Maximilian Deussing[3], Carla Palleis[4,5], Boris-Stephan Rauchmann[6,7], Franz-Josef Gildehaus[3], Simon Lindner[3], Charlotte Spitz[8], Nicolai Franzmeier[9], Karlheinz Baumann[10], Axel Rominger[3,11], Peter Bartenstein[3,12], Sibylle Ziegler[3,12], Alexander Drzezga[13,14,15], Gesine Respondek[16], Katharina Buerger[4,9], Robert Perneczky[4,7,12,17], Johannes Levin[4,5,12], Günter Höglinger[4,12,16,17], Jochen Herms[4,12,19], Christian Haass[1,4,12*] & Matthias Brendel[3,4,12*]

[1]Biomedical Center (BMC), Division of Metabolic Biochemistry, Faculty of Medicine, Ludwig-Maximilians-Universität München, Munich, Germany.
[2]CAS Key Laboratory of Brain Connectome and Manipulation, the Brain Cognition and Brain Disease Institute, Shenzhen Institutes of Advanced Technology, Chinese Academy of Sciences; Shenzhen-Hong Kong Institute of Brain Science-Shenzhen Fundamental Research Institutions, Shenzhen, 518055, China.
[3]Department of Nuclear Medicine, University Hospital of Munich, LMU Munich, Munich, Germany
[4]German Center for Neurodegenerative Diseases (DZNE) Munich, Munich, Germany
[5]Department of Neurology, University Hospital of Munich, LMU Munich, Munich, Germany
[6]Department of Radiology, University Hospital of Munich, LMU Munich, Germany
[7]Department of Psychiatry and Psychotherapy, University Hospital of Munich, LMU Munich, Germany
[8]Institut of Biochemistry and molecular biology, University of Augsburg, Augsburg
[9]Institute for Stroke and Dementia Research (ISD), University Hospital of Munich, LMU Munich, Munich, Germany
[10]Roche, Pharma Research and Early Development, NORD DTA / Neuroscience Discovery, Roche Innovation Center Basel, F. Hoffmann-La Roche Ltd., Grenzacherstrasse 124, CH-4070 Basel, Switzerland
[11]Department of Nuclear Medicine, University of Bern, Inselspital, Bern, Switzerland
[12]Munich Cluster for Systems Neurology (SyNergy), Munich, Germany
[13]Department of Nuclear Medicine, Faculty of Medicine and University Hospital Cologne, University of Cologne, Germany
[14]German Center for Neurodegenerative Diseases (DZNE), Bonn-Cologne, Germany
[15]Institute of Neuroscience and Medicine (INM-2), Molecular Organization of the Brain, Forschungszentrum Jülich, Germany
[16]Department of Neurology, Hannover Medical School, Hannover, Germany
[17]Ageing Epidemiology (AGE) Research Unit, School of Public Health, Imperial College, London, UK
[18]Department of Neurology, Technical University Munich, Munich, Germany
[19]Center for Neuropathology and Prion Research, Ludwig-Maximilians-University München, Munich, Germany

*Contributed equally.

To whom correspondence should be addressed: Christian.Haass@mail03.med.uni-muenchen.de & Matthias.Brendel@med.uni-muenchen.de

One Sentence Summary: Microglial impact on the FDG-PET signal

Keywords: Microglia, glucose, FDG-PET, β-amyloid, Trem2

Abstract

2-deoxy-2-[18F]fluoro-d-glucose positron-emission-tomography (FDG-PET) is widely used to study cerebral glucose metabolism. We investigated if the FDG-PET signal is directly influenced by microglial glucose uptake in mouse models and patients with neurodegenerative diseases. Using a novel approach for cell sorting after FDG injection we find that, at cellular resolution, microglia display higher glucose uptake than neuronal cell bodies and astrocytes. Notably, alterations in microglial glucose uptake are responsible for both, the FDG-PET signal decrease in Trem2-deficient mice and the FDG-PET signal increase in mouse models for amyloidosis. Thus, opposite microglial activation states determine the differential FDG uptake. Consistently, patients with Alzheimer's disease (n=12) and 4-repeat tauopathy (n=21) also exhibit a positive association between glucose uptake and microglial activity as determined by [18F]GE-180 18kDa translocator protein PET in preserved brain regions, indicating that the cerebral glucose uptake in humans is also significantly influenced by microglial activity. Our findings suggest that microglia activation states are responsible for FDG-PET signal alterations in patients with neurodegenerative diseases and mouse models for amyloidosis. Microglial activation states must therefore be considered when performing FDG-PET.

Introduction

Brain energy metabolism underlies complex mechanisms that can be altered during aging and in neurodegenerative conditions (*1*). FDG-PET measures of brain glucose uptake are widely used to detect regional patterns of hypometabolism typical for Alzheimer's disease (AD) patients (*2*). Consequently, FDG-PET was included as a measure of neuronal injury in the National Institutes on Aging-Alzheimer's Association (NIA-AA) research framework for AD (*3*). Regional reductions of glucose uptake are also used for the differential diagnosis of other neurodegenerative disorders, such as different etiologies of Parkinsonism (*4*). However, FDG-PET is lacking cellular resolution and the identity of the cell types contributing to the PET signal. It is assumed that the FDG-PET signal derives predominantly from neuronal synaptic activity (*5-7*). However, loss of function mutations in Trem2 (triggering receptor expressed on myeloid cells 2), a microglial gene involved in metabolism and activation (*8-11*), strongly impairs cerebral glucose uptake as measured by FDG-PET (*12*). On the contrary, an increased FDG-PET signal is frequently detected in independent mouse models for amyloidosis accompanied by microglial activation, where microglia is switching from homeostatic to disease associated microglia (DAM) (*13-15*). In a similar vein, FDG-PET studies in both autosomal dominant and sporadic AD have shown transient regional increases in the FDG-PET signal during early phases of β-amyloid (Aβ) accumulation (*16-20*), without causal explanation so far. We have shown that microglia activity is positively associated with cerebral FDG uptake in the aging and amyloid mouse models (*13, 21*). However, it is unclear if neurons and astrocytes increase their glucose uptake upon microglial activation, or if the increased FDG signal is directly derived from activated microglia. Similiarly, although it is well known that microglia increase their metabolic output in the setting of inflammation (*22, 23*), how much of the FDG-PET signal is related to activated microglia in disease conditions is largely unknow. We aimed to elucidate the cell specific uptake of glucose in brain. We hypothesized that microglia might be responsible for a much higher proportion of the brain's glucose uptake than hitherto estimated, and that FDG-PET signals may therefore reflect microglia activity.

Results

Pharmacological depletion of microglia ameliorates increased glucose uptake in mice with amyloidosis

First, we aimed to determine if and to what degree microglia are responsible for the elevated FDG-PET signal in the PS2APP mice (*24*), a mouse model for amyloidosis. To this end, microglia were depleted in PS2APP and wild-type (WT) mice by applying PLX5622 (*25*), an orally active, brain penetrant CSF1R inhibitor, at 1200 ppm in chow for seven weeks. Longitudinal FDG-, TSPO- and Aβ-PET measurements were performed at baseline and at the end of the study. Immunostaining using an antibody against the microglial-marker Iba1 confirmed a nearly complete depletion of microglia (-96%, $P < 0.0001$) in WT animals and a strong reduction of microglia (-66%, $P < 0.0001$) in PS2APP mice (Fig. S1A & B). Moreover, we confirm that PS2APP mice showed more microglia in both cortical and hippocampal regions due to amyloid-induced microgliosis (Fig. S1A & B). As expected, the PS2APP mice showed an elevated FDG-PET signal (*13*) in vehicle-treated groups when compared to WT (+17.6%, $P < 0.0001$) (Fig. 1A & B). PLX5622 treatment strongly reduced glucose uptake in PS2APP when compared to vehicle-treated PS2APP (-25.5%, $P < 0.0001$), even below the level of vehicle-treated WT animals (-12.4%, $P < 0.0001$) (Fig. 1A & B). This suggests that the FDG-PET signal elevation is substantially driven by microglia. To exclude anesthesia as a major confounder of our findings, we performed FDG-PET imaging after awake injection of FDG in PLX5622 or vehicle-treated PS2APP animals. PLX5622 treatment again strongly reduced glucose uptake in awake injected animals (-34%, $P = 0.0084$) (Fig. S2A & B). The FDG-PET signal in WT mice was also significantly reduced after PLX5622 treatment (-8.9%, $P = 0.0154$) (Fig. 1A & B), indicating that microglia also contribute significantly to glucose uptake even under physiological condition. To search for a potential correlation of microglia activation and cerebral glucose uptake, we performed TSPO-PET measurements. The TSPO-PET signal in PS2APP was likewise increased in vehicle-treated individuals when compared to vehicle-treated WT (+62.4%, $P < 0.0001$) but strongly decreased after PLX5622 treatment (-21.4%, $P < 0.0001$) (Fig. 1C & D). Changes from baseline between FDG-PET and TSPO-PET were

highly associated with each other (R = 0.6978, P = 0.0027) in PS2APP mice with PLX5622 treatment (Fig. 1E). To exclude potential neurotoxic effects after PLX5622 treatment, we performed terminal measures of synaptic density. Interestingly there were even higher levels of the synaptic density marker SV2A in PS2APP mice after microglia depletion (Fig. S1C & D). WT mice did not show differences between treatment and vehicle groups (Fig. S1C & D). The relatively short treatment duration did not lead to differences in fibrillar amyloidosis of PS2APP mice (SUVr: 0.92 ± 0.04 vs. 0.93 ± 0.02; P = n.s.) as measured by Aβ-PET (Fig. S2C & D). We conclude that the increased glucose uptake *in vivo* is completely ameliorated when large proportions of microglia cells are removed by CSF1R inhibition in PS2APP mice. Interestingly, even the basal glucose uptake in WT mice is reduced significantly upon microglia depletion. These data indicate that a relevant share of glucose uptake, as measured by *in vivo* FDG-PET, is related to microglia under physiological condition. Moreover, activated microglia drive the hitherto unexplained FDG-PET signal increase in the mouse model for amyloidosis.

Figure 1

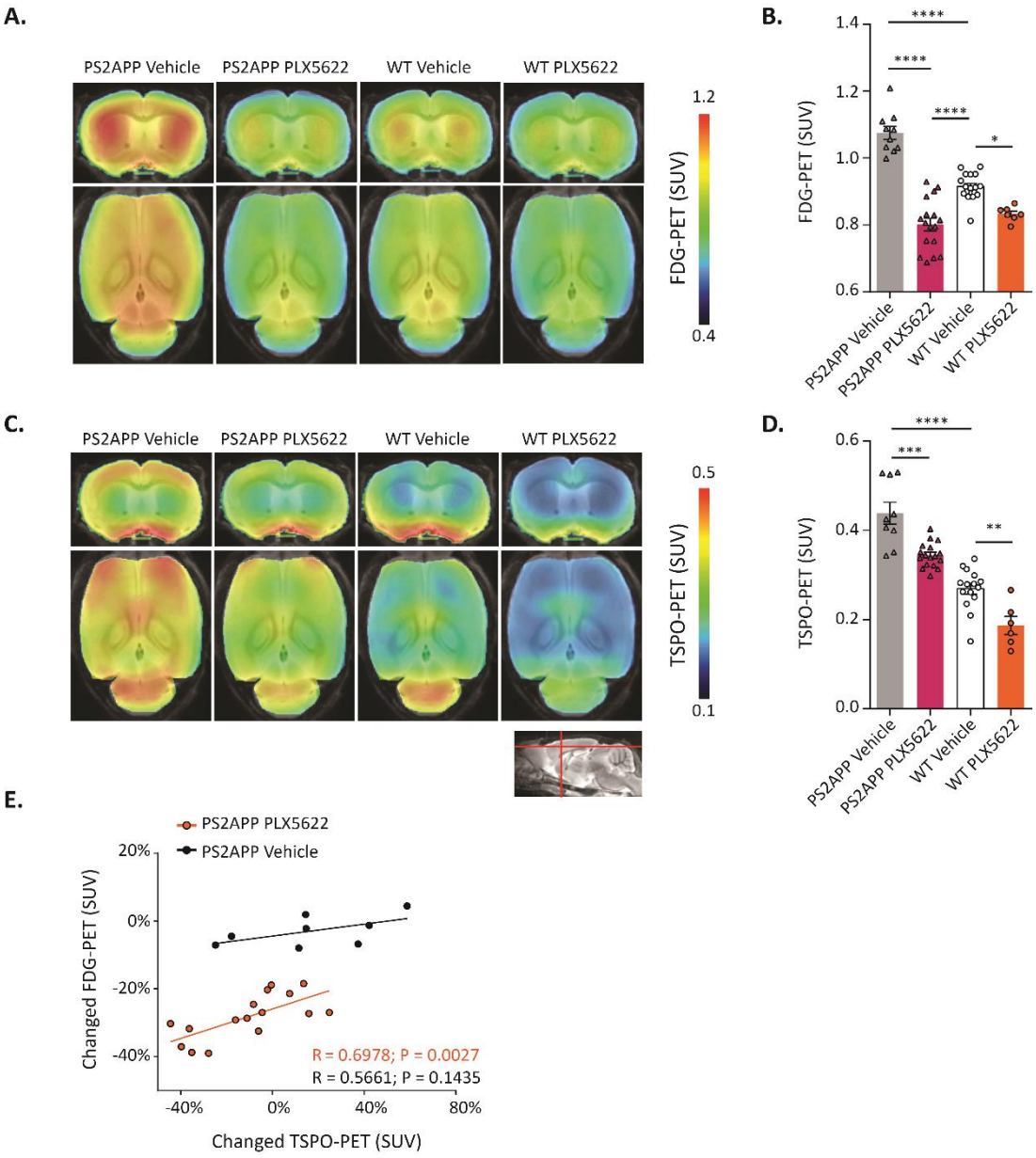

Figure 1 Pharmacological depletion of microglia ameliorates increased glucose uptake in mice with amyloidosis

(A). Coronal and axial slices show group averages of FDG-PET (SUV) per group projected upon a standard MRI T1 atlas. SUV: standardized uptake value.

(B). Quantification of cortical glucose uptake measured by *in vivo* FDG-PET. Mean ± s.e.m. of n = 7-17. One-way ANOVA P < 0.0001. *P < 0.05, ****P < 0.0001.

(C). Coronal and axial slices show group averages of TSPO-PET (SUV) per group projected upon a standard MRI T1 atlas.

(D). Quantification of cortical microglial activity measured by *in vivo* TSPO-PET. Mean ± s.e.m. of n = 6-17. One-way ANOVA P < 0.0001. **P < 0.01, ***P < 0.001, and ****P < 0.0001.

(E). Correlation of the changes from baseline between FDG-PET and TSPO-PET for PS2APP PLX5622 and vehicle-treated groups. PS2APP PLX5622 group: R = 0.6978, P = 0.0027; PS2APP vehicle: R = 0.5661, P = 0.1435.

Trem2 dependent amelioration of increased glucose uptake in mice with amyloidosis

We further confirmed our results using a Trem2-deficient mouse model for amyloidosis (*Trem2*$^{-/-}$ APPPS1) (*26*), where microglia showed an increased homeostatic signature and failed to acquire the DAM signature (*8, 27*). Glucose uptake and microglia activation were monitored longitudinally from 6 to 12 months of age using FDG- and TSPO-PET. Importantly, similar to the microglia depletion model, a significant reduction of longitudinal increases in cerebral glucose uptake was observed in *Trem2*$^{-/-}$ APPPS1 when compared to *Trem2*$^{+/+}$ APPPS1 (-13.4%, $P < 0.0001$) (Fig. 2A & B). At 12 months of age, glucose uptake was increased in *Trem2*$^{+/+}$ APPPS1 mice when compared to WT (+17.2%, $P < 0.0001$), but not in *Trem2*$^{-/-}$ APPPS1 (Fig. 2A & B). TSPO-PET data of these models were available from our previously published findings and showed a 4% TSPO-PET decrease at 6 months of age and a 20% TSPO-PET decrease at 12 months of age in *Trem2*$^{-/-}$ APPPS1 when compared to *Trem2*$^{+/+}$ APPPS1 (*9*). Longitudinal changes between FDG-PET and TSPO-PET were associated with each other ($R = 0.5913$, $P = 0.0333$) in APPPS1 mice (Fig. 2C). *Trem2*$^{-/-}$ mice showed the expected FDG-PET signal decrease (-10.6%, $P = 0.0023$) in comparison to WT mice, which was anticipated due to findings in the Trem2 p.T66M model (*28*). To exclude changes in cerebral blood flow as a major confounder of the correlations between glucose uptake and microglial activation, we performed dynamic FDG-PET imaging (0-60 min) and dynamic TSPO-PET imaging (0-90 min) in an aged cohort of *Trem2*$^{-/-}$ APPPS1 and *Trem2*$^{+/+}$ APPPS1 mice (15.5 months). Here, the calculated volumes of distribution (V_T) of FDG- and TSPO-PET were positively correlated with each other ($R = 0.7838$, $P = 0.0219$) (Fig. S3A-C). Thus, a genetically determined paradigm of microglia dysfunction confirmed the effects observed in the pharmacological microglia depletion model and suggests that the FDG-PET signal is substantially affected by the microglial activity state.

Figure 2

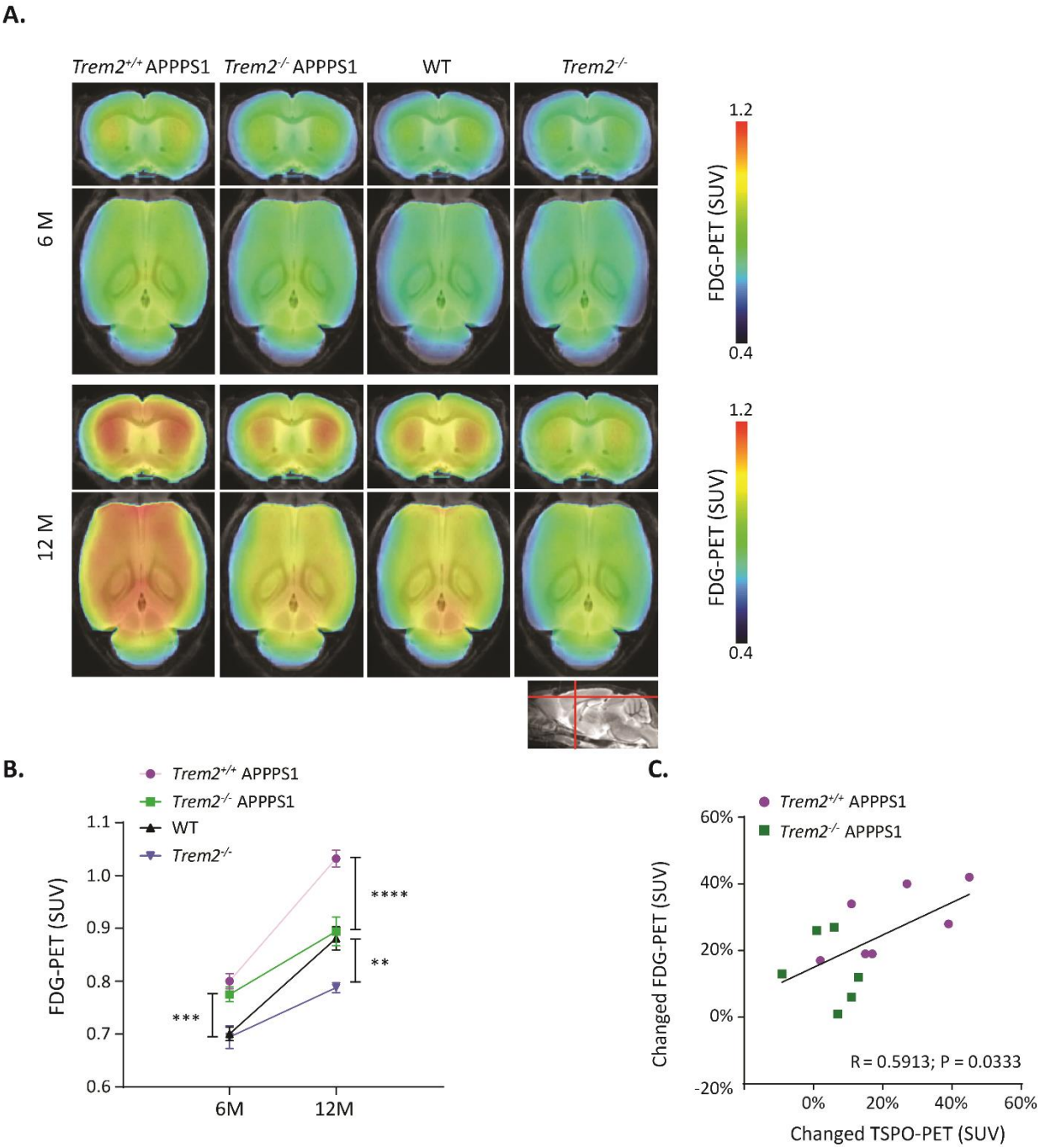

Figure 2 Trem2 dependent amelioration of the increased glucose uptake in mice with amyloidosis

(A). Coronal and axial slices show group averages of FDG-PET (SUV) per group projected upon a standard MRI T1 atlas.

(B). Quantification of cortical glucose uptake measured by *in vivo* FDG-PET at the ages of 6 and 12 months for *Trem2*$^{+/+}$ APPPS1, *Trem2*$^{-/-}$ APPPS1, WT, and *Trem2*$^{-/-}$ animals. Two-way ANOVA P = 0.0014. Bonferroni' multiple comparisons test, 6 months old (6M) *Trem2*$^{+/+}$APPPS1 vs. WT P = 0.0008; 12 months old (12M) *Trem2*$^{+/+}$ APPPS1 vs. *Trem2*$^{-/-}$ APPPS1 P < 0.0001; *Trem2*$^{+/+}$APPPS1 vs. WT P < 0.0001; WT vs. *Trem2*$^{-/-}$ P = 0.0023; *Trem2*$^{-/-}$ APPPS1 vs. WT nonsignificant. **P < 0.01, ***P < 0.001, and ****P < 0.0001.

(C). Correlation of the changes between FDG-PET and TSPO-PET in *Trem2*$^{+/+}$ APPPS1, *Trem2*$^{-/-}$ APPPS1 animals. R = 0.5913, P = 0.0333.

Microglia activation state determines the FDG uptake

Subsequently, based on the longitudinal PET data, we explored the proportions of FDG uptake in different cell types of the brain. To this end, we injected FDG in living mice, and 30 minutes post-injection, different cell types were isolated for gamma emission measures (Fig. 3A). The identities of the isolated cells were confirmed by western blots using antibodies against Tuj1, GFAP, and Iba1 (Fig. S4A). Gamma emission of specific cell types, as well as the depleted fractions, were subsequently recorded as a direct measure of *in vivo* glucose uptake and gamma counts were normalized to live cell numbers. Strikingly, microglia showed by far the highest FDG uptake (6.38E-7% ± 7.94E-8%), exceeding astrocyte uptake by 12-fold (5.17E-8% ± 4.68E-9%, $P < 0.0001$) and neuron uptake by 28-fold (2.21E-8% ± 2.04E-9%, $P < 0.0001$), after normalization to live cell number and to gamma emission from the whole brain (Fig. 3B). Depleted cell fractions confirmed these findings and indicated higher FDG uptake per individual cell in neuron-depleted (1.70E-7% ± 1.707E-8%, $P < 0.0001$) and astrocyte-depleted (2.27E-7% ± 1.25E-8%, $P < 0.0001$) fractions when compared to microglia-depleted fractions (5.09E-8% ± 3.99E-9%) (Fig. 3C). Dose-dependency of cellular FDG uptake was verified in neurons ($R = 0.9344$, $P = 0.0017$) (Fig. S4B), indicating that gamma emission is proportional to the actual glucose uptake.

Trem2 deficiency reduces metabolic fitness in microglia (*10*), and cerebral glucose uptake is reduced in a Trem2 loss of function mutant (*12*) and in *Trem2*$^{-/-}$ mice (Fig. 2A & B). To explore the cell-type-specific contribution of impaired glucose uptake, we isolated neurons, astrocytes, and microglia from *Trem2*$^{-/-}$ mice after FDG injection. Glucose uptake was reduced in *Trem2*$^{-/-}$ microglia when compared to microglia isolated from WT animals (1.91E-7% ± 4.91E-9% vs. 5.38E-7% ± 5.34E-8%, $P = 0.0001$) (Fig. 3D). In contrast, FDG uptake was unchanged in neurons and astrocytes from *Trem2*$^{-/-}$ animals indicating that the reduced glucose uptake in microglia may be responsible for the reduced FDG-PET signal in Trem2-deficient animals. Contrary to the FDG-PET decrease detected in Trem2-deficient models, FDG-PET increase is frequently observed in mouse models for amyloidosis (*13-15*). To further interrogate the

glucose uptake in an independent mouse model for amyloidosis, we measured FDG-PET in the knock-in model *App*$^{NL-G-F}$ (APPki) (*29*). Similar to PS2APP and APPPS1, we confirmed the cortical FDG-PET increase in APPki mice (*29*) (Fig. S5A & B). We then asked if the FDG-PET increase is driven by higher FDG uptake of microglia. Microglia isolated from APPki animals showed higher FDG uptake (1.01E-6 ± 9.65E-8%; per cell) when compared to microglia from WT animals (5.88E-7 ± 7.24E-8%, P = 0.0016; per cell) (Fig. 3E). No changes in FDG uptake were detected in neurons and astrocytes. Moreover, as a response to amyloid pathology, the expression of the glucose transporters Glut1 and Glut3 were increased in activated microglia (Fig. S4C). In contrast, the expression of Glut5, which is required for fructose uptake, was not significantly changed (Fig. S4C). Thus, the increased FDG uptake in activated microglia drives the FDG-PET increase in mouse models for amyloidosis (Fig. 3F). To validate PET results at a higher resolution, we performed *ex vivo* and *in vitro* autoradiography. APPki and WT mice indicated equivalent regions with off-target signals (i.e. ventricle, ependymal cells, Purkinje cells) for both tracers. Brain regions with an elevated signal in APPki mice when compared to WT mice were congruent for FDG-PET and TSPO-PET as quantified in the frontal cortex (*ex vivo* FDG: +44%, P < 0.0001; *in vitro* TSPO: +66%, P = 0.0017; *ex vivo* TSPO: +89%, P < 0.0001; Fig. S5C & D). In summary, the combination of *in vivo* FDG injection and cell sorting suggests that changes in FDG-PET signals in the investigated mouse models are predominantly driven by microglia activation.

Figure 3

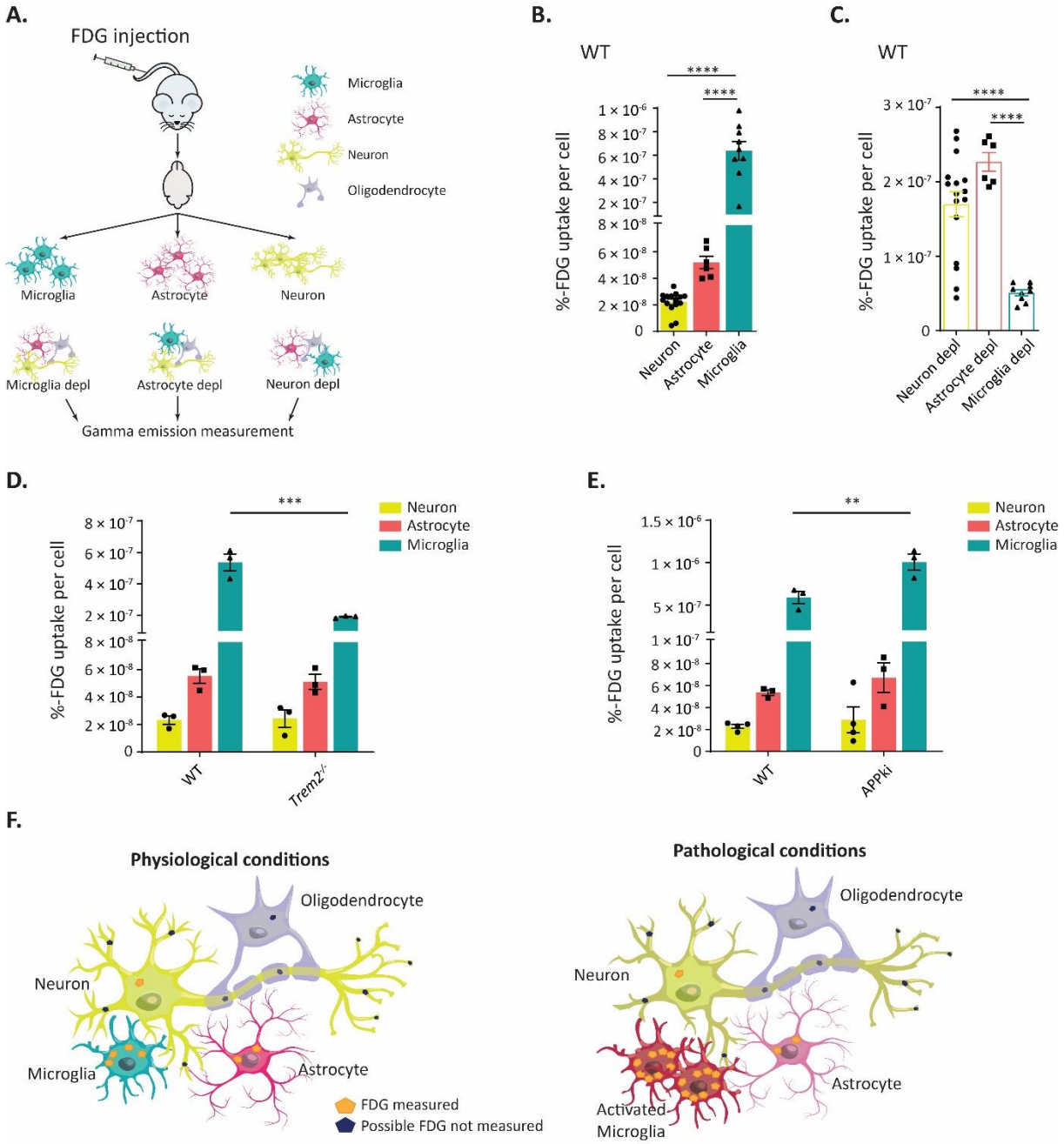

Figure 3 Microglia activation state determines the FDG uptake

(A). Schematic workflow of the combined cell sorting with gamma emission measurements.

(B). %-FDG uptake per cell in the isolated neuron, astrocyte, and microglia fractions from WT animals. Mean ± s.e.m. of n = 6-15. One-way ANOVA P < 0.0001; Tukey-corrected pair-wise post hoc tests. ****P < 0.0001; Neuron vs. astrocyte nonsignificant.

(C). %-FDG uptake per cell in isolated neuron depl (depl: depleted), astrocyte depl, and microglia depl fractions from WT animals. Mean ± s.e.m. of n = 6-15. One-way ANOVA P <0.0001; Tukey-corrected pair-wise post hoc tests. ****P < 0.0001; Neuron depl vs. astrocyte depl nonsignificant.

(D). %-FDG uptake per cell in the isolated neuron, astrocyte and microglia fractions from WT animals and *Trem2*$^{-/-}$ animals. Mean ± s.e.m. of n = 3. Two-way ANOVA P = 0.0004; Bonferroni' multiple comparisons test, ***P < 0.001.

(E). %-FDG uptake per cell in the isolated neuron, astrocyte and microglia fractions from WT animals and *App*$^{NL-G-F}$ animals (APPki). Mean ± s.e.m. of n = 3-4. Two-way ANOVA P = 0.0053; Bonferroni' multiple comparisons test, **P < 0.01.

(F). Schematic picture of FDG uptake in different cell types.

Regional positive association between microglial activation and glucose uptake in patients with Alzheimer's disease and 4-repeat tauopathies

To obtain evidence for a relationship between microglial activation and FDG-PET signal in humans, we investigated direct regional associations between TSPO-PET and FDG-PET in the human brain (Table 1, fig. S6). We expected a positive association between microglial activation, measured by TSPO-PET, and the FDG-PET signal, in previously described brain regions of preserved glucose uptake in patients with Aβ-positive AD and Aβ-negative 4-repeat tauopathies (*18*). Levels of TSPO-PET binding in cortical brain areas of these patients were elevated when compared to controls (Fig. S7A & B), confirming our previous data in a larger sample (*30*). In fact, the observed patterns of relative alterations in glucose uptake confirmed a parieto-occipital decrease and a frontal increase in Aβ-positive AD patients (Fig. 4A). Aβ-negative 4-repeat tauopathy patients showed minor decrease in the frontal lobe, but an unchanged FDG-PET signal in the parietal and temporal lobe (Fig. 4B). The relatively preserved frontal lobe in AD patients showed a significant positive association between TSPO- and FDG-PET quantification (Fig. 4C & E, $R = 0.6558$, $P = 0.0395$, partial correlation controlled for age and sex). Additionally, the relatively preserved parietal lobe in 4-repeat tauopathy patients likewise indicated a significant positive association between TSPO- and FDG-PET quantification (Fig. 4D & F, $R = 0.4716$, $P = 0.0415$, partial correlation controlled for age and sex). These data suggest that microglial activation is coupled to the elevated FDG-PET signal in regions without significant neuronal injury. Parietal and temporal brain regions in patients with AD, and frontal and temporal brain regions in 4-repeat tauopathy patients did not indicate significant associations between TSPO- and FDG-PET quantification (Fig. 4E & F), implying that neuronal function is still the primary modifier of FDG-PET results and microglial glucose uptake is an additive factor. This assumption was also supported by the magnitude of the correlation between TSPO- and FDG-PET in subregions of frontal, parietal, and temporal lobes, which was driven significantly by the degree of regional neuronal injury (Fig. 4G, $R = 0.346$, $P = 0.0289$). Validation analyses with dynamic TSPO-PET imaging in a small subsample of patients with 4-repeat tauopathies and application of different normalization

methods for PET mirrored the main results (Fig. S7C-F). Thus, our data suggest that the coupling between microglial activation and glucose uptake is changing with progressing neuronal dysfunction. Moreover, this supports our conclusion that microglia activity significantly modifies FDG-PET signal in brains/regions without obvious neurodegeneration. Thus, in humans, the FDG-PET signal is not only driven by neuronal activity but also determined by microglial activity, potentially explaining the transient regional FDG-PET elevation in the early stage of AD.

Table 1 Demographics and details of the human cohort

Demographics	4RT	AD pathophysiology	Controls (TSPO)	Controls (FDG)
n	21	12	14	18
Age (y)	69.2 ± 7.7	65.6 ± 8.7	70.3 ± 7.5	70.0 ± 11.1
Sex	10 ♀ / 11 ♂	8 ♀ / 4 ♂	7 ♀ / 7 ♂	7 ♀ / 11 ♂
Aβ positivity	0 (0%)	12 (100%)	0 (0%)	n.a.
rs6971	HAB: 15 / MAB: 6	HAB: 8 / MAB: 4	HAB: 6 / MAB: 8	n.a.
PSPRS	28.6 ± 12.5	24.4 ± 3.2	n.a.	n.a.
Disease duration (m)	23.0 ± 15.5	21.0 ± 14.2	n.a.	n.a.
MoCA	22.4 ± 4.5	14.4 ± 7.5	29.0 ± 1.0	30 ± 0
Time interval between FDG- and TSPO-PET (m)	1.9 ± 2.8	3.2 ± 3.4	n.a.	n.a.
Diagnosis	Possible 4RT n=6, Probable 4RT n=15	Typical AD n=7, AD-CBS n=5	n.a.	n.a.

AD = Alzheimer's disease; CBS = corticobasal syndrome; PSP = progressive supranuclear palsy; RS = Richardson syndrome; 4RT = 4-repeat tauopathies; TSPO = 18 kDa translocator protein; FDG = 2-deoxy-2-[18F]fluoro-d-glucose; PSPRS = PSP rating scale; y = years; m = months; n = sample size; MoCA = Montreal Cognitive Assessment; n.a. = not available; HAB = high affinity binder; MAB = medium affinity binder.

Figure 4

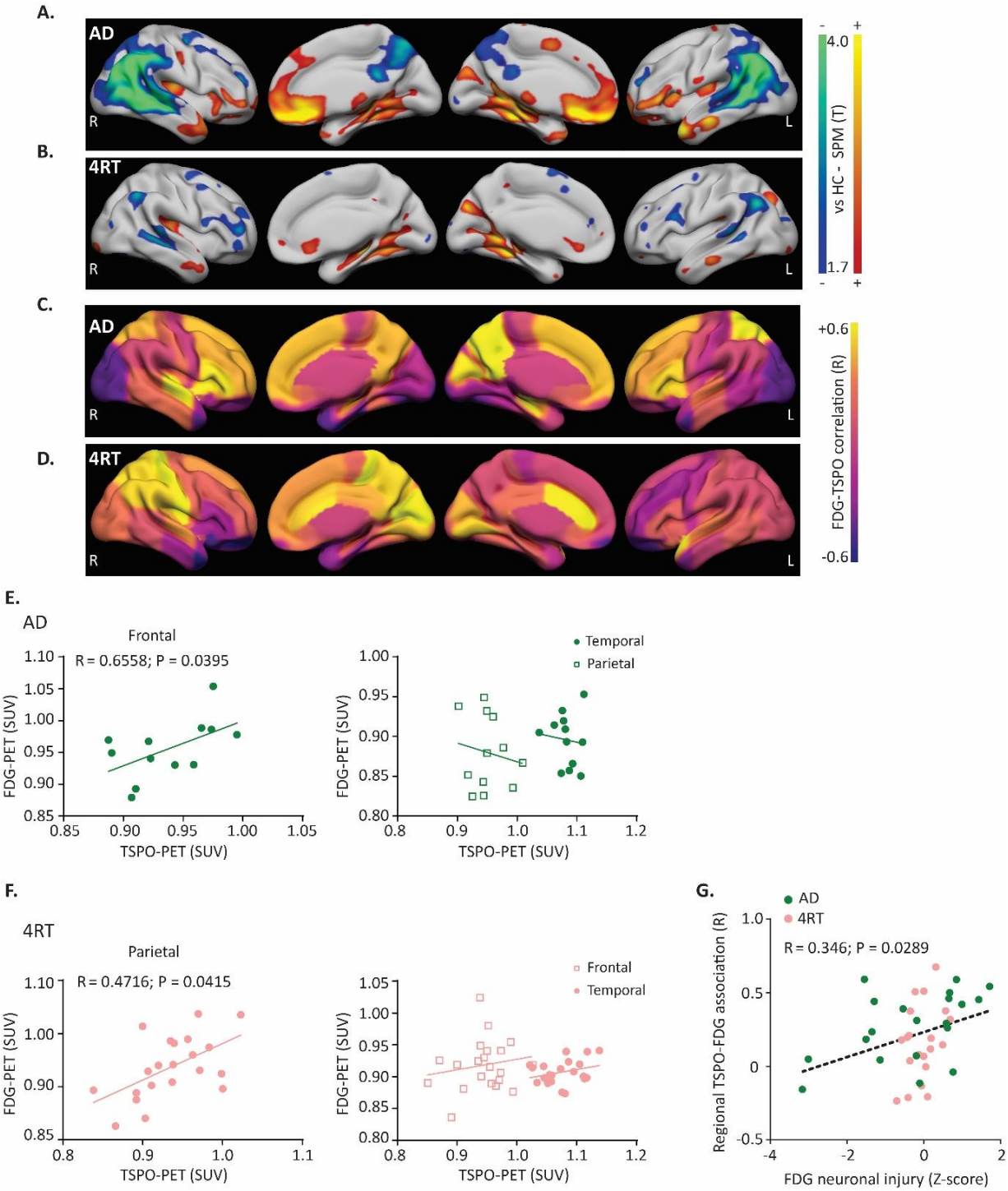

Figure 4 Preserved brain regions in patients with Alzheimer's disease and 4-repeat tauopathies show an association between microglia activation and glucose uptake

(A & B). Increases and decreases of FDG-PET in patients with Alzheimer's disease (AD, n = 12) (A) or 4-repeat tauopathies (4RT, n = 21) (B) when compared to healthy controls (n = 18). Surface projections are shown from lateral and medial views. SPM: statistical parametric mapping, T: T-score, R: right, L: left.

(C & D). Regional correlations between FDG-PET and TSPO-PET in patients with AD (C) or 4-repeat tauopathies (D). R values are reprojected on the cortical surface (n=56 cortical regions). R: Pearson's correlation coefficient.

(E & F). Correlation plots of FDG-PET and TSPO-PET in different regions of AD patients (E) and 4R tauopathy patients (F), adjusted for age and sex.
(G). Association between regional neuronal injury (defined by the FDG-PET Z-score) and the FDG-TSPO correlation. N = 20 regions per patient group.

Discussion

We provide direct evidence that the FDG-PET signal is substantially affected by microglial glucose uptake. We demonstrate that the FDG-PET signal increase in mouse models for amyloidosis is mainly driven by activated microglia. This is supported by our finding that the elevated FDG-PET signal in PS2APP was entirely abolished by PLX5622-induced microglia depletion. This observation is further supported by the positive correlation between the longitudinal changes of FDG-PET and the changes of the TSPO-PET signal in PLX5622-treated PS2APP mice. Our novel approach of FDG measurements after cell isolation confirmed that the activated microglia from APPki mice display higher glucose uptake compared to microglia isolated from WT animals. The novelty of this combinatorial approach consists in the possibilty to measure a direct surrogate of FDG uptake *in vivo* at the cellular resolution of microglia and other cell types. This is granted by hexokinase-mediated phosphorylation after the uptake phase, where FDG is trapped within the cells during the first minutes after injection. The gamma emission recordings were normalized to the number of live cells after isolation. Hence, the measured gamma emission is proportional to the actual glucose uptake at the cellular resolution *in vivo*. Thus, the increased glucose uptake in single activated microglia is attributable to the increased FDG-PET signal in mouse models of amyloidosis. We also showed that neuronal and astrocyte FDG uptake are similar between APPki and WT animals. We are aware that our isolation method misses the neuronal processes and synapses which may lead to underestimated neuronal FDG uptake in direct comparison of different cell types. In this regard axonal terminals are the sites of increased glucose utilization in response to neuronal firing (*31*), and a limitation of our study is the lack of resolution of synaptic glucose uptake. However, the combined consideration of cell sorting data and longitudinal microglia depletion relativized this limitation. PLX5622 treatment is likely to have little side-effects on neurons, as synaptic density is unchanged in WT animals between vehicle and PLX5622-treated groups. In fact, PLX5622 treatment even rescued the reduced synaptic density in PS2APP mice, implicating reduced synaptic pruning after microglia removal, which is in line with the earlier observed memory retention after PLX5622 treatment

(*32*). Thus, the amelioration of the FDG-PET signal increase upon microglial depletion in PS2APP mice occurs in the presence of a synaptic rescue, making an explanation of our findings by synaptic loss unlikely. Furthermore, since both hypermetabolism (*13, 14*) and reduced synaptic density (*33, 34*) are well-known features of mouse models of amyloidosis, it is less likely that the synaptic glucose uptake of neurons is another key contributor of the observed increased cerebral glucose uptake in APPki mice. On the other hand, the hyperactivate neurons around amyloid plaques could potentially contribute to the increased energy demand in models of amyloidosis (*35*). However, the direct measure of single cell microglial FDG emission argues that the increased microglial glucose uptake is at least one of the main contributors of the elevated FDG-PET signal in APPki animals.

We further confirmed the microglia dependent FDG-PET signal increase in mouse models of amyloidosis by showing that the elevated FDG-PET signal of APPPS1 mice is also relieved in mice lacking the microglial-gene Trem2. Trem2-deficient microglia express higher levels of homeostatic makers and fail to acquire the DAM signature when facing challenges like Aβ pathology (*8, 27, 36*). Furthermore, human iPSC-derived microglia expressing a Trem2 loss-of-function mutation display reduced oxidative phosphorylation and glycolytic capacity, and fail to switch from oxidative phosphorylation to aerobic glycolysis in response to pro-inflammatory stimuli (*37*). Glucose uptake is reduced in Trem2-deficient microglia but no uptake differences were observed in neurons or astrocytes. This suggests that the reduced glucose utilization in *Trem2*$^{-/-}$ microglia contribute to the FDG-PET signal decrease of Trem2-deficient mice at 12 months of age, similar to mice with a Trem2 loss-of-function mutation (*12*). Taken together, the altered glucose uptake of microglia is responsible for both the FDG-PET signal decrease in Trem2-deficient mice and the FDG-PET signal increase in mouse models of amyloidosis. The relevance of these findings is supported by the observation of elevated glucose metabolism-related proteins in microglia of AD patients (*38*).

Further studies need to address the consequence and the detailed mechanism of glucose metabolism regulation in microglia. Proteomic analysis indicated an up-regulation of carbohydrate metabolism in microglia from 12-month-old mice with amyloidosis (*39*). Our findings of an increased expression of the selective glucose transporters Glut1 and Glut3 in contrast to the decreased expression of the fructose transporter Glut5 in isolated microglia from mice with amyloidosis support this change in metabolic activity since Glut5 was described as a marker for resting microglia in humans and mice (*40, 41*). Consistent with this, Glut1 facilitates glucose uptake in microglia under inflammatory conditions (*42*). However, we note that the fate of glucose cannot be determined using FDG-PET. This needs to be considered since activated microglia and other activated immune cells are characterized by aerobic glycolysis whereas homeostatic microglia use oxidative phosphorylation with a much higher ATP yield (*43-45*). In addition, glucose is sequestrated away from ATP generation into glycogen in pro-inflammatory microglia (*46*). Therefore, we want to point out that our results suggest that microglia activity significantly influences the FDG-PET signal by changing the net glucose uptake, but these findings cannot be used to allow conclusions on energy metabolism in general. Interestingly, the amount of glucose taken up by microglia from WT mice appeared to be much higher when compared to astrocyte. Further studies need to elucidate if this energy stock is consumed by microglia themselves or by other cells. It is tempting to speculate that microglia might metabolically support neurons similar to the well know astrocyte-neuron lactate shuttle (*47*) and oligodendrocyte-neuron lactate shuttle (*48, 49*).

The impact of microglial FDG uptake on the overall FDG-PET signal in the face of brain pathology (i.e., amyloidosis) may partly explain previous reports of positive associations between PET-assessed Aβ levels and FDG-PET in the human brain at early disease stages of AD (*16-20*). Previous studies have argued that i) higher regional brain activity may either drive Aβ accumulation (*50, 51*) or ii) that Aβ accumulation induces neuronal hyperactivity/hyperexcitability (*52, 53*), thus resulting in FDG-PET increases. Our sample size of AD patients was not large enough to test for interaction effects of the sigmoidal increases of fibrillar Aβ pathology during AD progression (*54*) on the association between microglial

activation during the time course of AD (*55*) and FDG-PET. Nonetheless, we find a positive direct association between elevated TSPO-PET and FDG-PET signal increases in brain regions with amyloidosis and without significant neuronal injury in AD patients even when using a very conservative PET quantification apporach. Taken together with our preclinical data, we conclude that microglia, which are activated during amyloidosis (*56, 57*), stimulate glucose uptake and thus further drive the increase of FDG-PET signal. Importantly, we show that this link between microglial activation and glucose uptake is not restricted to amyloidosis since a positive association between FDG-PET and TSPO-PET could be replicated in 4-repeat tauopathy patients. Thus, our findings of elevated FDG uptake apprear to be a general phenomenon of microglial response. As a limitation, it needs to be considered that most imaging data were acquired in a late static window which can be biased by changes in cerebral blood flow. Thus, although we were able to validate our main findings by dynamic imaging in mice and in parts of the human data, some degree of the observed correlations between FDG-PET and TSPO-PET could still be explained by communtated changes in cerebral blood flow. We note that the human brain comprises a higher neuron to non-neuronal cell ratio when compared to a weight normalized brain of rodents (*58*). Thus, the relative fraction of glucose uptake by microglia is probably less pronounced in humans when compared to rodents. In this regard, FDG uptake and microglial activity did not correlate in brain regions with significant neuronal injury, indicating that neuronal activity is still the most relevant driving force of the human FDG-PET signal once neurodegeneration becomes apparent. However, the combined translational data suggests a general contribution of microglia to the FDG-PET signal across neurodegenerative conditions. Consequently, elevated microglial FDG uptake at early stages of diseases determines larger parts of the FDG-PET signal and this could explain why structural atrophy is not necessarily accompanied by metabolic decline (*18*). Since the FDG-PET signals also refect microglial activity, the microglial activation states must be recognized when using FDG-PET imaging for diagnostic work-up and scientific trials.

Materials and Methods

Animals and treatment

All animal experiments were performed in compliance with the National Guidelines for Animal Protection, Germany and with the approval of the regional animal committee (Regierung von Oberbayern) overseen by a veterinarian. Animals were housed in a temperature- and humidity-controlled environment with 12h light-dark cycle, with free access to food and water. Homozygous female PS2APP (APPswe/PS2) mice (*24*) and age-matched wild-type (WT) were used for pharmacological depletion of microglia by CSF1R inhibition (*25*). Mice received FDG-PET, TSPO-PET, and β-amyloid-PET (Aβ-PET) at 9.5 months of age and were randomized into treatment or vehicle groups per cage at 10 months of age. CSF1R inhibition was performed by administration of PLX5622 (1200 ppm) for seven weeks, and follow-up PET scans were performed in the last week of treatment. Brain extraction for immunohistochemistry analyses was performed on the last day of treatment. Serial FDG-PET and TSPO-PET scans of female APPPS1 (APPPS1-21) mice (*59*) and age-matched WT with intact or deficient Trem2 (*Trem2*$^{+/+}$ APPPS1, *Trem2*$^{-/-}$ APPPS1, *Trem2*$^{+/+}$, *Trem2*$^{-/-}$) were analyzed at 6 and 12 months of age (*26*). WT and *Trem2*$^{-/-}$ between 7 and 11 months of age served for isolation experiments of microglia, astrocytes, and neurons. *App*$^{NL-G-F}$(APPki) mice (*60, 61*) underwent FDG-PET at 10 months of age. APPki mice at 10 months of age served for isolation experiments of microglia, astrocytes, and neurons.

Small animal PET

All small animal positron emission tomography (μPET) procedures followed an established standardized protocol for radiochemistry, acquisition, and post-processing (*13, 62*). In brief, ^{18}F-FDG μPET (FDG-PET) with an emission window of 30-60 mins post-injection was used to measure cerebral glucose uptake, ^{18}F-GE-180 TSPO μPET (TSPO-PET) with an emission window of 60-90 mins post-injection was used to measure cerebral microglial activity, and ^{18}F-

florbetaben β-amyloid µPET (Aβ-PET) with an emission window of 30-60 mins post-injection was used for assessment of fibrillar cerebral amyloidosis. All analyses were performed by PMOD (V3.5, PMOD Technologies, Basel, Switzerland) using tracer specific templates for spatial normalization (*62*). Normalization of injected activity was performed by a two-step process for FDG-PET and TSPO-PET to consider global and region-specific effects. First, standardized uptake values (SUV) were generated either by conventional division by the injected dose and multiplication by the bodyweight (FDG-PET) or by the previously validated myocardium correction method (*63*) (TSPO-PET). Second, intragroup stabilization was performed by centering SUV values to established intracerebral reference tissues (*13, 26, 64*), to allow robust correlation analyses between different tracers. Normalization of injected activity for Aβ-PET in PS2APP mice was performed by reference region scaling (*13*). µPET estimates deriving from a standardized bilateral neocortical target volume of interest (19 mm^3) (*65*) were extracted from all individual mice. All small animal PET experiments were performed with isoflurane anesthesia (1.5% at time of tracer injection and during imaging; delivery 3.5 L/min). To exclude anesthesia as a major confounder of our findings, we performed a validation experiment of FDG-PET imaging with awake injection of the tracer, using n=4 PLX5622 treated PS2APP and n=3 vehicle treated PS2APP mice at the follow-up time-point (under treatment). Isoflurane anesthesia was induced 15 min after injection of FDG in order to avoid effects of isoflurane during the FDG uptake phase. PET imaging was performed from 30 to 60 min p.i. as in the main experiment. Analysis of FDG-PET images of the awake injection experiment was equal to the main experiment. To exclude changes in cerebral blood flow as a major confounder of the correlations between glucose uptake and microglial activation, we performed dynamic FDG-PET imaging (0-60 min) and dynamic TSPO-PET imaging (0-90 min) in a validation cohort of n=4 *Trem2*$^{+/+}$ APPPS1 and n=4 *Trem2*$^{-/-}$ APPPS1 mice at the age of 15.5 months. Framing was 3x10s, 3x30s, 8x60s, 10x300s for FDG-PET and 3x10s, 3x30s, 8x60s, 10x300s, 3x600s for TSPO-PET with all other reconstruction parameters remaining equal. Coregistration was performed via the late imaging windows as in the main experiment with application of the saved transformations to the full dynamic data file (*62*). We calculated volume

of distribution (V_T) images with an image derived input function (*66*) using the methodology described by Logan et al. implemented in PMOD (*67*). The plasma curve was obtained from a standardized bilateral VOI placed in both carotid arteries. A maximum error of 10% and a V_T threshold of 0 were selected for modelling of the full dynamic imaging data. The VOI-based analysis of V_T images was performed equal to the SUV and SUVr PET analyses. Cortical V_T values of FDG-PET and TSPO-PET of all mice were correlated with each other to test if the observed association between glucose uptake and microglial activation also holds true in cerebral blood flow adjusted quantification.

Autoradiography

Ex vivo and *in vitro* autoradiography experiments were performed to validate PET results at a higher resolution. n=2-3 *App*$^{NL-G-F}$ mice and WT mice at 16-18 months of age were used and n=2-4 randomly selected brain sections per animal were analyzed for quantification. Autoradiography protocols were similar to previous reports of our group and detailed descriptions are provided there (*13, 68, 69*). In brief, we used 20 µm sagittal sections obtained via cutting in a Leica CM 1510-1 Cryostat (Leica Microsystems, Nussloch Germany), thermally equilibrated at – 20 ºC for 30 min prior to cutting. The procedure was performed after injection of ~15 MBq ^{18}F-FDG or ~15 MBq ^{18}F-GE-180 and the brain was extracted after stopping the circulation in the middle of the PET imaging window (45 min p.i. for ^{18}F-FDG; 75 min p.i. for ^{18}F-GE-180). *In vitro* autoradiography with ^{18}F-GE-180 was performed on the same sections that were used for *ex vivo* FDG autoradiography in order to prove that the FDG signal corresponds to sites of microglial activation. Here, the section was incubated with ^{18}F-GE-180 at a concentration of ~2 nM for 60 min, followed by washing with Tris-HCl buffer (50 nM, pH 7.4). *Ex vivo* and *in vitro* autoradiography sections were placed on Fujifilm BAS cassette2 2025 imaging plates. The plates were exposed for six hours and then scanned at 25 µm resolution with the Raytest equipment (CR-35-BIO, Dürr Medical, Germany). Resulting images were analyzed with AIDA image analysing software, V4.50 (Raytest GmbH, Straubenhardt,

Germany). For all analyzed sections, we used manually drawn cerebellar and frontal cortical regions of interest and we calculated a frontal cortex to cerebellum ratio. The operator was blind to the genotype, but we note that the genotype specific differences in tracer uptake between *App*$^{NL-G-F}$ and WT mice were likely identified by visual inspection. The cortex to cerebellum ratios were compared between *App*$^{NL-G-F}$ and WT mice by an unpaired Student's t-test for each autoradiography modality.

Human PET

Twelve patients with fibrillar amyloidosis (AD continuum and corticobasal syndrome) and 21 patients with possible or probable 4-repeat tauopathies (corticobasal syndrome and progressive supranuclear palsy) were available for within subject analysis of FDG-PET and TSPO-PET. Control data derived from 18 (FDG-PET) and 14 (TSPO-PET) age- and sex-matched individuals without objective memory impairment and with intact motor function (Table 1). Patients were enrolled in the interdisciplinary AD study "Activity of Cerebral Networks, Amyloid and Microglia in Aging and AD (ActiGliA)" and were scanned at the Department of Nuclear Medicine, LMU, using a Biograph 64 PET/CT scanner (Siemens, Erlangen, Germany). Aβ-PET was performed in all patients using ^{18}F-flutemetamol. PET acquisition and PET data analyses (ethics-applications: 17-569 & 17-755) were approved by the local institutional ethics committee (LMU Munich) and the German radiation protection authorities. All participants provided written informed consent before the PET scans. Before each PET acquisition, a low-dose CT scan was performed for attenuation correction. Emission data of FDG-PET were acquired from 30 to 50 minutes post-injection according to the EANM protocol (*70*). Emission data of TSPO-PET were acquired from 60 to 80 minutes (*71*) after the injection of 191 ± 10 MBq ^{18}F-GE-180 as an intravenous bolus. The specific activity was >1500 GBq/μmol at the end of radiosynthesis, and the injected mass was 0.13 ± 0.05 nmol. Emission data of Aβ-PET were acquired from 90 to 110 minutes after injection of 190 ± 12 MBq ^{18}F-flutemetamol. Images were reconstructed using a 3-dimensional ordered subsets expectation maximization algorithm

(16 iterations, 4 subsets, 4 mm gaussian filter) with a matrix size of 336 × 336 × 109, and a voxel size of 1.018 × 1.018 × 2.027 mm. Standard corrections for attenuation, scatter, decay, and random counts were applied.

FDG-PET and TSPO-PET data were analyzed using PMOD. Spatial normalization was performed to tracer specific templates in the Montreal Neurology Institute (MNI) space analogous to mouse data processing. All images were normalized by global mean scaling and smoothed with a Gaussian filter of 6x6x6 mm to account for intersubject differences in anatomy. The Hammers atlas was used for region definition (*72*), and bilobar frontal, temporal and parietal cortical target regions were defined as described previously (*73*). Regional associations of FDG-PET and TSPO-PET in predefined lobar volumes of interest were calculated by Pearson's coefficient of correlation (R). Correlation coefficients of single cortical Hammers atlas regions (n=56) were computed for visualization purposes and correlation analyses with neuronal injury. The degree of regional neuronal injury (expressed as FDG z-score in patients vs. controls) was correlated with the degree of association between FDG-PET and TSPO-PET for all single brain regions of the Hammers atlas above a volume of 10 mm^3 (n=20). For the purpose of cerebral blood flow adjusted validation, we analyzed a subset of n=5 patients with 4R-tauopathies that received dynamic TSPO-PET imaging (0-90 min). We analyzed the agreement between distribution volume ratios of TSPO-PET (DVR, simplified reference tissue modelling 2 (*74*)) and the primarily used 60-80 min SUVr quantification of TSPO-PET for frontal, temporal and parietal regions of interest. Additionally, we analyzed the correlation between TSPO-PET DVR (n=5) and SUVr (n=21) with FDG-PET SUVr in the parietal lobe, to test if the agreement between glucose uptake and microglial activation is also present when a kinetic modelling quantification is applied to TSPO-PET. Furthermore, in both analyses, we confirmed the results obtained by scaling through the global mean (subsequently performed after DVR calculation and for generation of SUVr) with normalization by the cerebellum as a reference region (DVR and SUVr). In addition to the relative quantification approaches, we compared TSPO-PET SUV quantification (60-80 min time-window) of all

target regions (frontal, temporal, parietal) between patients with AD and 4-repeat tauopathies against controls.

Aβ-PET was assessed by a visual read (one expert reader), and the decision of Aβ-positivity/negativity was supported by a software-driven approach implemented in HERMES Gold (V4.17, HERMES Medical Solutions AB, Stockholm, Sweden). One positive evaluated target region (frontal, temporal, parietal, posterior cingulate) defined the scan as positive.

Immunofluorescence

After conducting the last µPET scans, each mouse was perfused transcardially with ice-cold phosphate-buffered saline (PBS). The right hemibrains were frozen at -80°C until further use. The left hemibrains were immersion-fixed with 4% paraformaldehyde overnight at 4°C. Subsequently, 50 µm-thick hemispherical parasagittal slices were prepared using a vibratome (VT1000S, Leica, Germany). Three to five paramedian slices from each animal were used in a free-floating immunofluorescence labeling approach. The sections were incubated in 2% Triton X-100 in PBS (2% PBST) at 4°C for 16-20 hours for permeabilization, following by blocking with 10% normal goat serum (NGS) in 0.3% PBST for 2-3 h at room temperature. The slices were incubated with primary antibodies diluted in a blocking solution of 5% NGS in 0.3% PBST for 48h (SV2A; 1:200, #ab32942; Abcam, Germany) or 24h (Iba1; 1:200, #019-19741; FUJIFILM Wako Chemicals. USA) at 4°C. After primary target labeling, unbound antibodies were removed by three consecutive washing steps with PBS for 15 minutes each before secondary antibody goat anti-rabbit AlexaFlour®488 (#A11008; Thermo Fisher Scientific, Germany) incubation in 1:1000 dilutions at room temperature for 4 h. For nuclear counterstain, DAPI (#D9542; Sigma-Aldrich, Germany) was applied to the free-floating sections in a 1:1000 PBS dilution for 20 minutes at room temperature. Finally, slices were rewashed and mounted on Superfrost-plus® slides (Thermo Fisher Scientific, Germany) using Fluorescence Mounting Medium (#S302380-2, Agilent Dako, Germany) with #1.5H high-precision imaging glass coverslips (#48393-059, VWR, Germany).

Image acquisition and analysis

Synaptic images were acquired with constant imaging settings using a Zeiss LSM780 confocal system (Zeiss, Germany) equipped with a Plan-Apochromat 40X (NA 1.4, DIC M27, oil immersion) objective and a user interface provided with the ZEN Black software. For quantification of synaptic puncta, nine high-resolution 2D planes of ROIs of (75.87 x 75.87) μm^2 from the hippocampus, Stratum radiatum of the CA1, were randomly sampled among 2-3 slices of each animal. For the examination of neocortical regions, we randomly sampled nine high-resolution 2D planes with ROIs of (101.21 x 101.21) μm^2 in the SSC LII/LIII, which was located dorsally from the inspected hippocampal area in all 2-3 slices per animal. Image properties were given as follows: pixel dwell = 0.39 µs, lateral resolution = 0.037 µm, image depth = 16-bit, dpi = 2048. Single images were processed by custom IJ2-written macro scripts in the Fiji/ImageJ, which included background subtraction, thresholding with binarization, and the 'Analyze Particles' command to obtain single measures of puncta count.

For microglial counts in PLX5622 or vehicle-treated animals, we used the LSM780 confocal system equipped with a Plan-Apochromat 20X/0.8 M27 objective. Wide horizontal image stacks were acquired covering either the somatosensory cortex (SSC) with adjacent neocortical areas of size (1889.32 x 944.66 x 15) μm^3 or the whole hippocampal CA of size (1889.32 x 472.33 x 15) μm^3 of each respective brain slice in one frame (z-steps = 1 µm, pixel dwell = 0.64 µs, lateral resolution = 0.231 µm, image depth = 12-bit, dpi = 1024). These large image stacks were imported into Fiji/ImageJ, where 3 VOIs per region of size 400 µm were sampled, projected in maximum intensity mode. Then microglial cell bodies were counted manually. Final microglia density values were expressed as the quotient of Iba1-positive microglia and the frame size. For this analysis, we compared three slices of the brains from 3 animals out of each cohort.

Mouse brain dissociation

Adult Brain Dissociation Kit, mouse, and rat (Miltenyi Biotec, 130-107-677) was used for adult mouse brain dissociation according to the manufacturer's instructions. Adult mouse brains were dissected out and briefly washed with PBS. The brains were cut into eight pieces and dissociated with enzyme mix 1 and 2 using gentleMACS™ Octo Dissociator (Miltenyi Biotec, 130-096-427). The dissociated cell suspension was applied to pre-wet 100 µm Cell Strainer (Falcon, 352360). The cell pellet was resuspended using cold PBS and cold debris removal solution. Cold PBS was gently overlaid on the cell suspension. Centrifuge at 4°C and 3000×g for 10 minutes with acceleration and deceleration at 5. The two top phages were removed entirely. The cell pellets were collected and resuspended with 1 ml cold red blood cell removal solution followed by 10 minutes incubation. Cell pellets were collected for further applications.

Isolation of neurons

Neuron Isolation Kit, mouse (Miltenyi Biotec, 130-115-390), was used according to the manufacturer's instructions. The prepared cell pellets were resuspended in 80 µl of PBS-0.5% BSA (Bovine Serum Albumin) buffer per 10^7 total cells. 20 µL of Non-Neuronal Cells Biotin-Antibody Cocktail was added and incubated for 5 minutes in the dark at 4°C. Cells were washed and centrifuge at 300×g for 5 minutes. Cell pellets were again resuspended in 80 µL of PBS-0.5% BSA buffer per 10^7 total cells. 20 µL of Anti-Biotin MicroBeads were added and incubated for 10 minutes in the dark at 4°C. The volume was adjusted to 500 µl per 10^7 total cells with PBS-0.5% BSA buffer and then proceed to magnetic separation. The pre-wet LS columns (Miltenyi Biotec, 130-042-401) were placed at QuadroMACS™ Separator (Miltenyi Biotec, 130-090-976). The cell suspensions were applied onto the column. The columns were washed with 2 × 1 ml PBS-0.5% BSA buffer. The flow-through containing the unlabeled cells were collected as the neuron-enriched fractions. The columns were removed from the magnetic field, and the non-neuronal cells were flashed out using 3 ml of PBS-0.5% BSA buffer.

Isolation of astrocytes

Adult Brain Dissociation Kit, mouse, and rat (Miltenyi Biotec, 130-107-677) was used according to the manufacturer's instructions. The prepared cell pellets were resuspended in 80 µl of AstroMACS separation buffer (Miltenyi Biotec, 130-117-336) per 10^7 total cells. 10 µL of FcR blocking reagent was added and incubated for 10 minutes in the dark at 4°C. 10 µL of Anti-ACSA-2 MicroBeads was added and incubated for 15 minutes in the dark at 4°C. Cells were washed by adding 1 mL of AstroMACS separation buffer and centrifuge at 300×g for 5 minutes. Cell pellets were resuspended using 500 µL of AstroMACS separation buffer. The pre-wet MS columns (Miltenyi Biotec, 130-042-201) were placed at OctoMACS Separator (Miltenyi Biotec, 130-042-109). The cell suspensions were applied onto the column, followed by washing with 3 × 500 µL of AstroMACS separation buffer. The flow-through was collected containing non-astrocytic cells as an astrocyte-depleted fraction. The columns were removed from the magnetic field, and the astrocytes were flashed out using 3 ml of AstroMACS separation buffer.

Isolation of microglia

Microglia were isolated from animals using CD11b microbeads (Miltenyi Biotec, 130-093-634) and a MACS separation system (Miltenyi Biotec) as described (*75, 76*). The prepared cell pellets were resuspended in 90 µl of PBS-0.5% BSA buffer per 10^7 total cells. 10 µl of CD11b microBeads per 10^7 total cells were added and incubated for 15 minutes in the dark at 4°C. Cells were washed by adding 1−2 mL of buffer per 10^7 cells and centrifuge at 300×g for 10 minutes. The cell pellets were resuspended in 500 µl of PBS-0.5% BSA. The pre-wet LS columns were placed at QuadroMACS™ Separator. The cell suspensions were applied onto the column. The columns were washed with 3 × 3 ml PBS-0.5% BSA buffer. The flow-through containing the unlabeled cells were collected as the microglia-depleted fractions. The columns

were removed from the magnetic field, and microglia were flashed out using 5 ml of PBS-0.5% BSA buffer.

Gamma emission measurements

Radioactivity concentrations of cell pellets were measured in a gamma counter (Cobra Quantum 5002, Packard) cross-calibrated to the activity in the whole brain, with decay-correction to time of tracer injection for final activity calculations.

RNA isolation and quantitative real-time PCR

Total RNA was isolated from 400.000 microglial cells using the RNeasy Plus Micro Kit (Qiagen, Cat No./ID: 74034) according to the manufacturers protocol. RNA quality and concentration were determined with the Bioanalyzer 2100 (Agilent). RNA integrity numbers varied between 8.3 and 9.3. cDNA was synthesized from 200 ng of total RNA using the M-MLV reverse transcriptase (Promega, cat No. M1701) with random nonamer primers for 1 h at 42°C followed by 15 min heat inactivation at 95 °C. Quantification was performed with the 7500 Fast Real Time PCR System (Applied Biosystems) using the following probes targeting glucose transporters (Integrated DNA Technologies): Slc2a1 (Mm.PT.58.7590689), Slc2a2 (Mm.PT.58.45874027), Slc2a3 (Mm.PT.58.30464830), Slc2a4 (Mm.PT.58.9683859), Slc2a5 (Mm.PT.58.41178805). Relative expression of target genes was normalized against endogenous controls HSP90ab1 (Mm.PT.58.43472263.g) and Actb (4352341E, Thermo Scientific). Slc2a2 and Slc2a4 were below the detection limit in the isolated microglia.

Statistical analysis

Data are presented as mean ± s.e.m unless otherwise stated. Statistical significance was calculated by one-way analysis of variance (ANOVA) followed by Bonferroni post hoc test for group-wise comparisons or Mann-Whitney test unless otherwise stated. When comparing

multiple groups, two-way ANOVA was applied, followed by Bonferroni's multiple comparisons tests unless otherwise stated. The correlation between FDG-PET and TSPO-PET was analyzed by simple linear regression. Age and sex were adjusted as indicated.

References

1. S. Camandola, M. P. Mattson, Brain metabolism in health, aging, and neurodegeneration. *EMBO J* **36**, 1474-1492 (2017).
2. C. R. Jack, Jr. *et al.*, Tracking pathophysiological processes in Alzheimer's disease: an updated hypothetical model of dynamic biomarkers. *The Lancet. Neurology* **12**, 207-216 (2013).
3. C. R. Jack, Jr. *et al.*, NIA-AA Research Framework: Toward a biological definition of Alzheimer's disease. *Alzheimers Dement* **14**, 535-562 (2018).
4. C. C. Tang *et al.*, Differential diagnosis of parkinsonism: a metabolic imaging study using pattern analysis. *The Lancet. Neurology* **9**, 149-158 (2010).
5. L. Sokoloff, Sites and mechanisms of function-related changes in energy metabolism in the nervous system. *Dev Neurosci* **15**, 194-206 (1993).
6. L. Sokoloff, Energetics of functional activation in neural tissues. *Neurochem Res* **24**, 321-329 (1999).
7. L. Sokoloff *et al.*, The [14C]deoxyglucose method for the measurement of local cerebral glucose utilization: theory, procedure, and normal values in the conscious and anesthetized albino rat. *J Neurochem* **28**, 897-916 (1977).
8. S. Krasemann *et al.*, The TREM2-APOE Pathway Drives the Transcriptional Phenotype of Dysfunctional Microglia in Neurodegenerative Diseases. *Immunity* **47**, 566-581.e569 (2017).
9. S. Parhizkar *et al.*, Loss of TREM2 function increases amyloid seeding but reduces plaque-associated ApoE. *Nature neuroscience* **22**, 191-204 (2019).
10. T. K. Ulland *et al.*, TREM2 Maintains Microglial Metabolic Fitness in Alzheimer's Disease. *Cell* **170**, 649-663.e613 (2017).
11. Y. Wang *et al.*, TREM2 lipid sensing sustains the microglial response in an Alzheimer's disease model. *Cell* **160**, 1061-1071 (2015).
12. G. Kleinberger *et al.*, The FTD-like syndrome causing TREM2 T66M mutation impairs microglia function, brain perfusion, and glucose metabolism. *The EMBO journal* **36**, 1837-1853 (2017).
13. M. Brendel *et al.*, Glial Activation and Glucose Metabolism in a Transgenic Amyloid Mouse Model: A Triple-Tracer PET Study. *J Nucl Med* **57**, 954-960 (2016).
14. X. Y. Li *et al.*, Age- and Brain Region-Specific Changes of Glucose Metabolic Disorder, Learning, and Memory Dysfunction in Early Alzheimer's Disease Assessed in APP/PS1 Transgenic Mice Using (18)F-FDG-PET. *Int J Mol Sci* **17**, (2016).
15. G. Poisnel *et al.*, Increased regional cerebral glucose uptake in an APP/PS1 model of Alzheimer's disease. *Neurobiol Aging* **33**, 1995-2005 (2012).
16. T. L. Benzinger *et al.*, Regional variability of imaging biomarkers in autosomal dominant Alzheimer's disease. *Proc Natl Acad Sci U S A* **110**, E4502-4509 (2013).
17. A. D. Cohen *et al.*, Basal cerebral metabolism may modulate the cognitive effects of Abeta in mild cognitive impairment: an example of brain reserve. *J Neurosci* **29**, 14770-14778 (2009).
18. B. A. Gordon *et al.*, Spatial patterns of neuroimaging biomarker change in individuals from families with autosomal dominant Alzheimer's disease: a longitudinal study. *Lancet Neurol* **17**, 241-250 (2018).
19. H. Oh, C. Habeck, C. Madison, W. Jagust, Covarying alterations in Abeta deposition, glucose metabolism, and gray matter volume in cognitively normal elderly. *Hum Brain Mapp* **35**, 297-308 (2014).
20. H. Oh, C. Madison, S. Baker, G. Rabinovici, W. Jagust, Dynamic relationships between age, amyloid-beta deposition, and glucose metabolism link to the regional vulnerability to Alzheimer's disease. *Brain* **139**, 2275-2289 (2016).
21. M. Brendel *et al.*, Time Courses of Cortical Glucose Metabolism and Microglial Activity Across the Life Span of Wild-Type Mice: A PET Study. *J Nucl Med* **58**, 1984-1990 (2017).
22. S. H. Baik *et al.*, A Breakdown in Metabolic Reprogramming Causes Microglia Dysfunction in Alzheimer's Disease. *Cell Metabolism* **30**, 493-507.e496 (2019).

23. C. Lauro, C. Limatola, Metabolic Reprograming of Microglia in the Regulation of the Innate Inflammatory Response. *Frontiers in immunology* **11**, 493-493 (2020).
24. J. G. Richards *et al.*, PS2APP transgenic mice, coexpressing hPS2mut and hAPPswe, show age-related cognitive deficits associated with discrete brain amyloid deposition and inflammation. *J Neurosci* **23**, 8989-9003 (2003).
25. E. Spangenberg *et al.*, Sustained microglial depletion with CSF1R inhibitor impairs parenchymal plaque development in an Alzheimer's disease model. *Nat Commun* **10**, 3758 (2019).
26. S. Parhizkar *et al.*, Loss of TREM2 function increases amyloid seeding but reduces plaque-associated ApoE. *Nature neuroscience* **22**, 191-204 (2019).
27. H. Keren-Shaul *et al.*, A Unique Microglia Type Associated with Restricting Development of Alzheimer's Disease. *Cell* **169**, 1276-1290.e1217 (2017).
28. G. Kleinberger *et al.*, The FTD-like syndrome causing TREM2 T66M mutation impairs microglia function, brain perfusion, and glucose metabolism. *EMBO J* **36**, 1837-1853 (2017).
29. T. Saito *et al.*, Single App knock-in mouse models of Alzheimer's disease. *Nature neuroscience* **17**, 661-663 (2014).
30. C. Palleis *et al.*, In Vivo Assessment of Neuroinflammation in 4-Repeat Tauopathies. *Mov Disord*, (2020).
31. M. Kadekaro, A. M. Crane, L. Sokoloff, Differential effects of electrical stimulation of sciatic nerve on metabolic activity in spinal cord and dorsal root ganglion in the rat. *Proc Natl Acad Sci U S A* **82**, 6010-6013 (1985).
32. C. Wang *et al.*, Microglia mediate forgetting via complement-dependent synaptic elimination. *Science* **367**, 688-694 (2020).
33. T. L. Spires, B. T. Hyman, Neuronal structure is altered by amyloid plaques. *Rev Neurosci* **15**, 267-278 (2004).
34. J. Tsai, J. Grutzendler, K. Duff, W. B. Gan, Fibrillar amyloid deposition leads to local synaptic abnormalities and breakage of neuronal branches. *Nat Neurosci* **7**, 1181-1183 (2004).
35. M. A. Busche *et al.*, Clusters of hyperactive neurons near amyloid plaques in a mouse model of Alzheimer's disease. *Science* **321**, 1686-1689 (2008).
36. F. Mazaheri *et al.*, TREM2 deficiency impairs chemotaxis and microglial responses to neuronal injury. *EMBO reports* **18**, 1186-1198 (2017).
37. T. M. Piers *et al.*, A locked immunometabolic switch underlies TREM2 R47H loss of function in human iPSC-derived microglia. *The FASEB Journal* **34**, 2436-2450 (2020).
38. E. C. B. Johnson *et al.*, Large-scale proteomic analysis of Alzheimer's disease brain and cerebrospinal fluid reveals early changes in energy metabolism associated with microglia and astrocyte activation. *Nat Med* **26**, 769-780 (2020).
39. L. Sebastian Monasor *et al.*, Fibrillar Abeta triggers microglial proteome alterations and dysfunction in Alzheimer mouse models. *Elife* **9**, (2020).
40. Y. Horikoshi *et al.*, Human GLUT5 immunolabeling is useful for evaluating microglial status in neuropathological study using paraffin sections. *Acta Neuropathol* **105**, 157-162 (2003).
41. V. Haage *et al.*, Comprehensive gene expression meta-analysis identifies signature genes that distinguish microglia from peripheral monocytes/macrophages in health and glioma. *Acta Neuropathol Commun* **7**, 20 (2019).
42. L. Wang *et al.*, Glucose transporter 1 critically controls microglial activation through facilitating glycolysis. *Mol Neurodegener* **14**, 2 (2019).
43. R. Orihuela, C. A. McPherson, G. J. Harry, Microglial M1/M2 polarization and metabolic states. *Br J Pharmacol* **173**, 649-665 (2016).
44. E. L. Pearce, E. J. Pearce, Metabolic pathways in immune cell activation and quiescence. *Immunity* **38**, 633-643 (2013).
45. E. L. Pearce, M. C. Poffenberger, C. H. Chang, R. G. Jones, Fueling immunity: insights into metabolism and lymphocyte function. *Science* **342**, 1242454 (2013).

46. P. S. Minhas *et al.*, Restoring metabolism of myeloid cells reverses cognitive decline in ageing. *Nature*, (2021).
47. L. Pellerin, P. J. Magistretti, Glutamate uptake into astrocytes stimulates aerobic glycolysis: a mechanism coupling neuronal activity to glucose utilization. *Proceedings of the National Academy of Sciences* **91**, 10625-10629 (1994).
48. U. Fünfschilling *et al.*, Glycolytic oligodendrocytes maintain myelin and long-term axonal integrity. *Nature* **485**, 517-521 (2012).
49. Y. Lee *et al.*, Oligodendroglia metabolically support axons and contribute to neurodegeneration. *Nature* **487**, 443-448 (2012).
50. R. L. Buckner *et al.*, Cortical hubs revealed by intrinsic functional connectivity: mapping, assessment of stability, and relation to Alzheimer's disease. *J Neurosci* **29**, 1860-1873 (2009).
51. J. R. Cirrito *et al.*, Synaptic activity regulates interstitial fluid amyloid-beta levels in vivo. *Neuron* **48**, 913-922 (2005).
52. B. Zott *et al.*, A vicious cycle of beta amyloid-dependent neuronal hyperactivation. *Science* **365**, 559-565 (2019).
53. Q. Liu, X. Xie, R. J. Lukas, P. A. St John, J. Wu, A novel nicotinic mechanism underlies beta-amyloid-induced neuronal hyperexcitation. *J Neurosci* **33**, 7253-7263 (2013).
54. C. R. Jack, Jr., D. M. Holtzman, Biomarker modeling of Alzheimer's disease. *Neuron* **80**, 1347-1358 (2013).
55. Z. Fan, D. J. Brooks, A. Okello, P. Edison, An early and late peak in microglial activation in Alzheimer's disease trajectory. *Brain : a journal of neurology* **140**, 792-803 (2017).
56. M. Dani *et al.*, Microglial activation correlates in vivo with both tau and amyloid in Alzheimer's disease. *Brain : a journal of neurology* **141**, 2740-2754 (2018).
57. Z. Cai, M. D. Hussain, L. J. Yan, Microglia, neuroinflammation, and beta-amyloid protein in Alzheimer's disease. *Int J Neurosci* **124**, 307-321 (2014).
58. S. Herculano-Houzel, The human brain in numbers: a linearly scaled-up primate brain. *Front Hum Neurosci* **3**, 31 (2009).
59. R. Radde *et al.*, Abeta42-driven cerebral amyloidosis in transgenic mice reveals early and robust pathology. *EMBO Rep* **7**, 940-946 (2006).
60. A. Masuda *et al.*, Cognitive deficits in single App knock-in mouse models. *Neurobiol Learn Mem* **135**, 73-82 (2016).
61. T. Saito *et al.*, Single App knock-in mouse models of Alzheimer's disease. *Nature neuroscience* **17**, 661-663 (2014).
62. F. Overhoff *et al.*, Automated Spatial Brain Normalization and Hindbrain White Matter Reference Tissue Give Improved [(18)F]-Florbetaben PET Quantitation in Alzheimer's Model Mice. *Frontiers in neuroscience* **10**, 45 (2016).
63. M. Deussing *et al.*, Coupling between physiological TSPO expression in brain and myocardium allows stabilization of late-phase cerebral [(18)F]GE180 PET quantification. *NeuroImage* **165**, 83-91 (2017).
64. C. Sacher *et al.*, Longitudinal PET Monitoring of Amyloidosis and Microglial Activation in a Second Generation Amyloid-beta Mouse Model. *Journal of nuclear medicine : official publication, Society of Nuclear Medicine*, (2019).
65. A. Rominger *et al.*, Longitudinal assessment of cerebral beta-amyloid deposition in mice overexpressing Swedish mutant beta-amyloid precursor protein using 18F-florbetaben PET. *J Nucl Med* **54**, 1127-1134 (2013).
66. W. K. Schiffer, M. M. Mirrione, S. L. Dewey, Optimizing experimental protocols for quantitative behavioral imaging with 18F-FDG in rodents. *Journal of nuclear medicine : official publication, Society of Nuclear Medicine* **48**, 277-287 (2007).
67. J. Logan *et al.*, Graphical analysis of reversible radioligand binding from time-activity measurements applied to [N-11C-methyl]-(-)-cocaine PET studies in human subjects. *Journal of cerebral blood flow and metabolism : official journal of the International Society of Cerebral Blood Flow and Metabolism* **10**, 740-747 (1990).

68. M. Brendel *et al.*, Amyloid-PET predicts inhibition of de novo plaque formation upon chronic gamma-secretase modulator treatment. *Mol Psychiatry* **20**, 1179-1187 (2015).
69. M. Brendel *et al.*, Small-Animal PET Imaging of Tau Pathology with 18F-THK5117 in 2 Transgenic Mouse Models. *J Nucl Med* **57**, 792-798 (2016).
70. A. Varrone *et al.*, EANM procedure guidelines for PET brain imaging using [18F]FDG, version 2. *European journal of nuclear medicine and molecular imaging* **36**, 2103-2110 (2009).
71. N. L. Albert *et al.*, TSPO PET for glioma imaging using the novel ligand (18)F-GE-180: first results in patients with glioblastoma. *Eur J Nucl Med Mol Imaging* **44**, 2230-2238 (2017).
72. A. Hammers *et al.*, Three-dimensional maximum probability atlas of the human brain, with particular reference to the temporal lobe. *Hum Brain Mapp* **19**, 224-247 (2003).
73. L. Beyer *et al.*, Early-phase [(18)F]PI-2620 tau-PET imaging as a surrogate marker of neuronal injury. *European journal of nuclear medicine and molecular imaging*, (2020).
74. Y. Wu, R. E. Carson, Noise reduction in the simplified reference tissue model for neuroreceptor functional imaging. *Journal of cerebral blood flow and metabolism : official journal of the International Society of Cerebral Blood Flow and Metabolism* **22**, 1440-1452 (2002).
75. X. Xiang *et al.*, The Trem2 R47H Alzheimer's risk variant impairs splicing and reduces Trem2 mRNA and protein in mice but not in humans. *Mol Neurodegener* **13**, 49 (2018).
76. A. V. Colombo *et al.*, Microbiota-derived short chain fatty acids modulate microglia and promote Abeta plaque deposition. *Elife* **10**, (2021).

Acknowledgments

The study was supported by the FöFoLe Program of the Faculty of Medicine of the Ludwig Maximilian University, Munich (grant to M.B.). This work was funded by the Deutsche Forschungsgemeinschaft (DFG, German Research Foundation) to A.R. and M.B. – project numbers BR4580/1-1/ RO5194/1-1. This project was also supported by the German Center for Neurodegenerative Diseases (DZNE, DescribePSP Study), the German Parkinson's Association (DPG, ProPSP Study), and the Hirnliga e.V. (Manfred-Strohscheer-Stiftung). P.B., G.U.H., C.H., J.H., and R.P. were supported by the Deutsche Forschungsgemeinschaft (DFG, German Research Foundation) under Germany's Excellence Strategy within the framework of the Munich Cluster for Systems Neurology (EXC 2145 SyNergy – ID 390857198). C.H. is supported by a Koselleck Project HA1737/16-1 and the Helmholtz-Gemeinschaft Zukunftsthema 'Immunology and Inflammation' (ZT-0027). G.U.H. was also funded by the NOMIS foundation (FTLD project). The Lüneburg Heritage has supported the work of C.P. We thank all of our patients, their care-givers, cyclotron, radiochemistry, and the PET imaging crew. GE Healthcare made GE-180 cassettes available through an early-access model. The authors thank Plexxikon Inc. for providing PLX5622. We thank Mathias Jucker for providing the APPPS1 mice and to Takashi Saito and Takaomi C. Saido for providing the *App*$^{NL\text{-}G\text{-}F}$mice.

Conflict of interest

M.B. received speaker honoraria from GE healthcare and LMI and is an advisor of LMI. G.U.H. received research support from GE Healthcare and Neuropore; has ongoing research collaborations with Orion and Prothena; serves as a consultant for AbbVie, AlzProtect, Asceneuron, Biogen, Biohaven, Lundbeck, Novartis, Roche, Sanofi, UCB; received honoraria for scientific presentations from AbbVie, Biogen, Roche, Teva, UCB, and Zambon; and holds a patent on PERK Activation for the Treatment of Neurodegenerative Diseases (PCT/EP2015/068734). C.H. is the chief scientific advisor of ISAR biosciences and collaborates with DENALI therapeutics. R.P. is on the advisory board for Biogen, has consulted for Eli Lilly, is a grant recipient from Janssen Pharmaceutica and Boehringer Ingelheim, and has received speaker honoraria from Janssen-Cilag, Pfizer, and Biogen. J.L. reports speaker fees from Bayer Vital, consulting fees from Axon Neuroscience, author fees from Thieme medical publishers and W. Kohlhammer GmbH medical publishers, non-financial support from Abbvie and compensation for duty as part-time CMO from MODAG GmbH, all outside the submitted work. G.R. is on the advisory board for UCB and received honorara for scientific presentations from Biogen. A.D. received research support: Siemens Healthineers, Life Molecular Imaging, GE Healthcare, AVID Radiopharmaceuticals, has Speaker Honorary/Advisory Boards: Siemens Healthineers, Sanofi, GE Healthcare, Stock of Siemens

Healthineers, and a patent pending for 18F-PSMA7 (PSMA PET imaging tracer). All other authors do not report a conflict of interest.

Author contributions

J.H., C.H., X.X. and M.B. conceived the study and analyzed the results. X.X. and M.B. wrote the manuscript with help from C.H. and further input from all co-authors. X.X. and K.W. performed isolation experiments and gamma emission recordings. S.R., S.T. and M.W. isolated microglia for quantitative PCR and S.L. performed RNA analyses. T.W., G.B., F.E., and M.D. performed the small animal PET experiments and small animal PET data analyses. A.Z. performed kinetic modeling analyses. T.B., Y.S., and N.B. performed immunohistochemistry analyses. FJ.G. and S.L. performed PET tracer synthesis and analyses. N.F. interpreted human PET data and contributed to their analysis. C.P., B.R., K.B., R.P., G.R. J.L., and G.H. recruited patients and contributed to human PET analyses and interpretation. A.R., P.B., S.Z. and A.D. interpreted glucose uptake and FDG-PET in conjunction with rodent and human data. T.B., Y.S., N.B., and J.H interpreted immunohistochemistry. C.S. has drawn the schematic figures.

Supplementary Materials

Supplementary figure 1

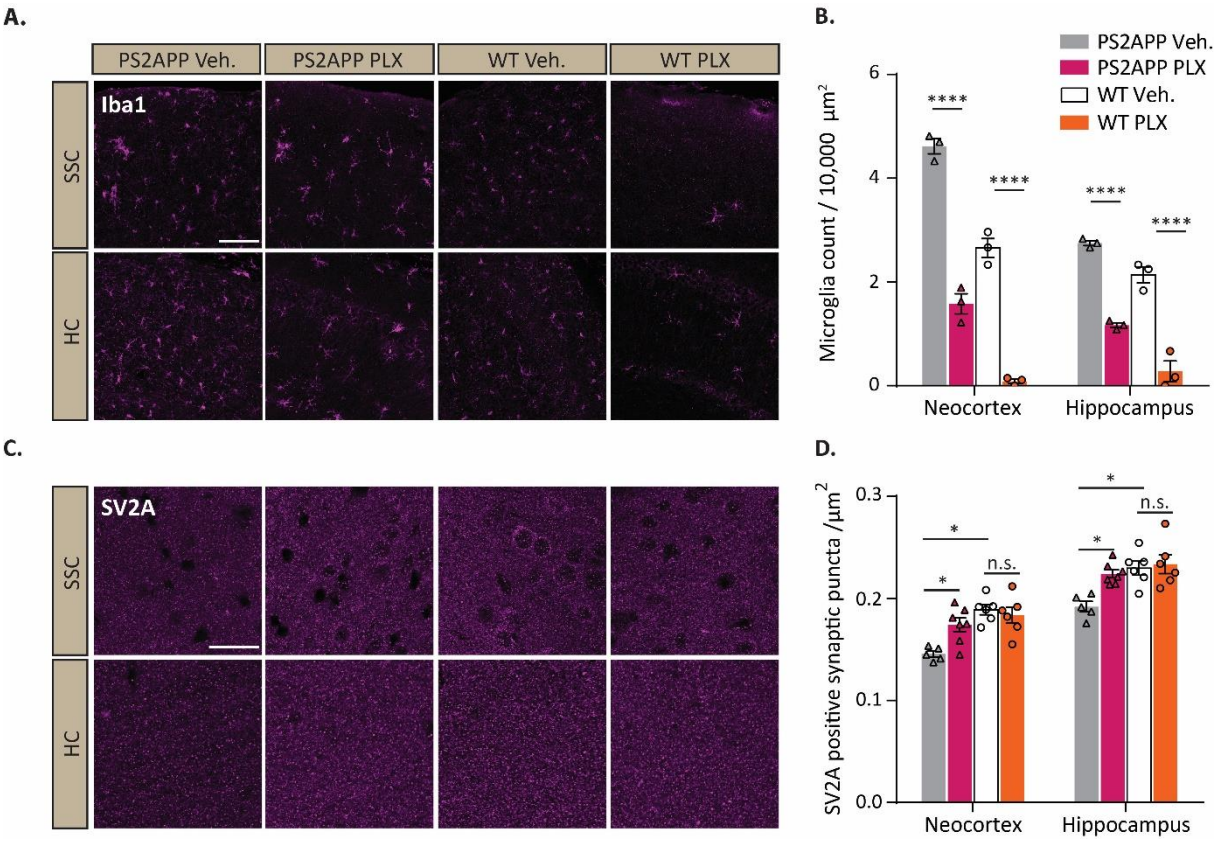

Fig. S1 Microglia density and synaptic density after PLX5622 treatment

(A). Representative images of microglia marker Iba1 immunostaining. Scale bar, 100 µm.
(B). Microglia counts in the neocortex and hippocampus. Mean ± s.e.m. of n = 3. Two-way ANOVA P = 0.0002; Tukey-corrected pair-wise post hoc tests, ****P < 0.0001.
(C). Representative images of synaptic density marker SV2A immunostaining. Scale bar, 20 µm.
(D). SV2A positive synaptic puncta area coverage in the neocortex and hippocampus. Mean ± s.e.m. of n = 5. Two-way ANOVA P = 0.1635, n.s.: non-significant; Tukey-corrected pair-wise post hoc tests, *P < 0.05.

Supplementary figure 2

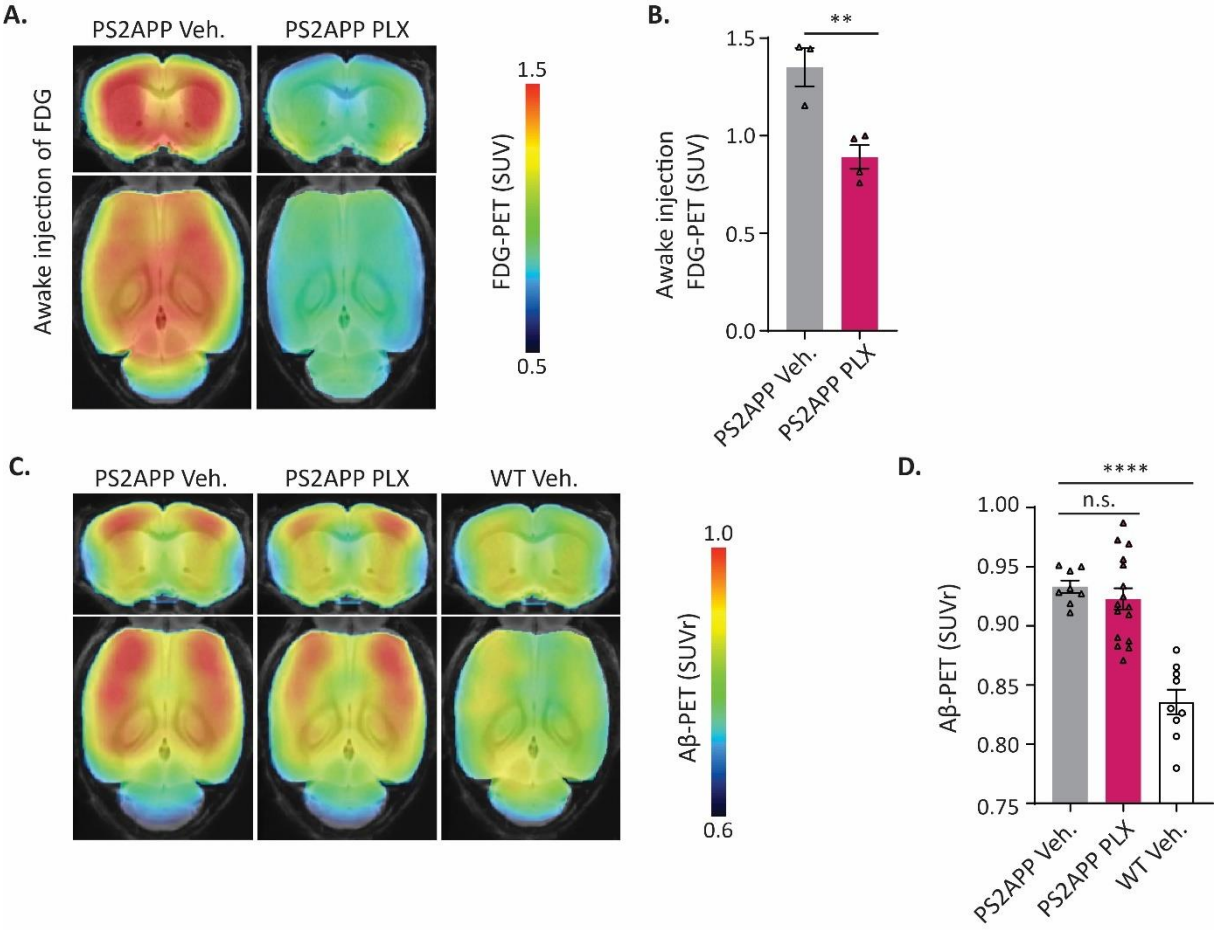

Fig. S2 FDG and Aβ-PET after PLX5622 treatment

(A). Coronal and axial slices show group averages of FDG-PET (SUV) of awake injected animals.
(B). Quantification of cortical glucose uptake in awake animals. Mean ± s.e.m. of n = 3-4. Unpaired two-tailed t test P = 0.0084.
(C). Coronal and axial slices show standardized uptake value ratio maps of Aβ-PET projected upon a standard MRI template. Aβ, β-amyloid.
(D). Quantification of cortical Aβ load measured by *in vivo* Aβ-PET. Mean ± s.e.m. of n = 8-16. One-way ANOVA; Bonferroni post hoc tests. n.s.: non-significant; ****P < 0.0001.

Supplementary figure 3

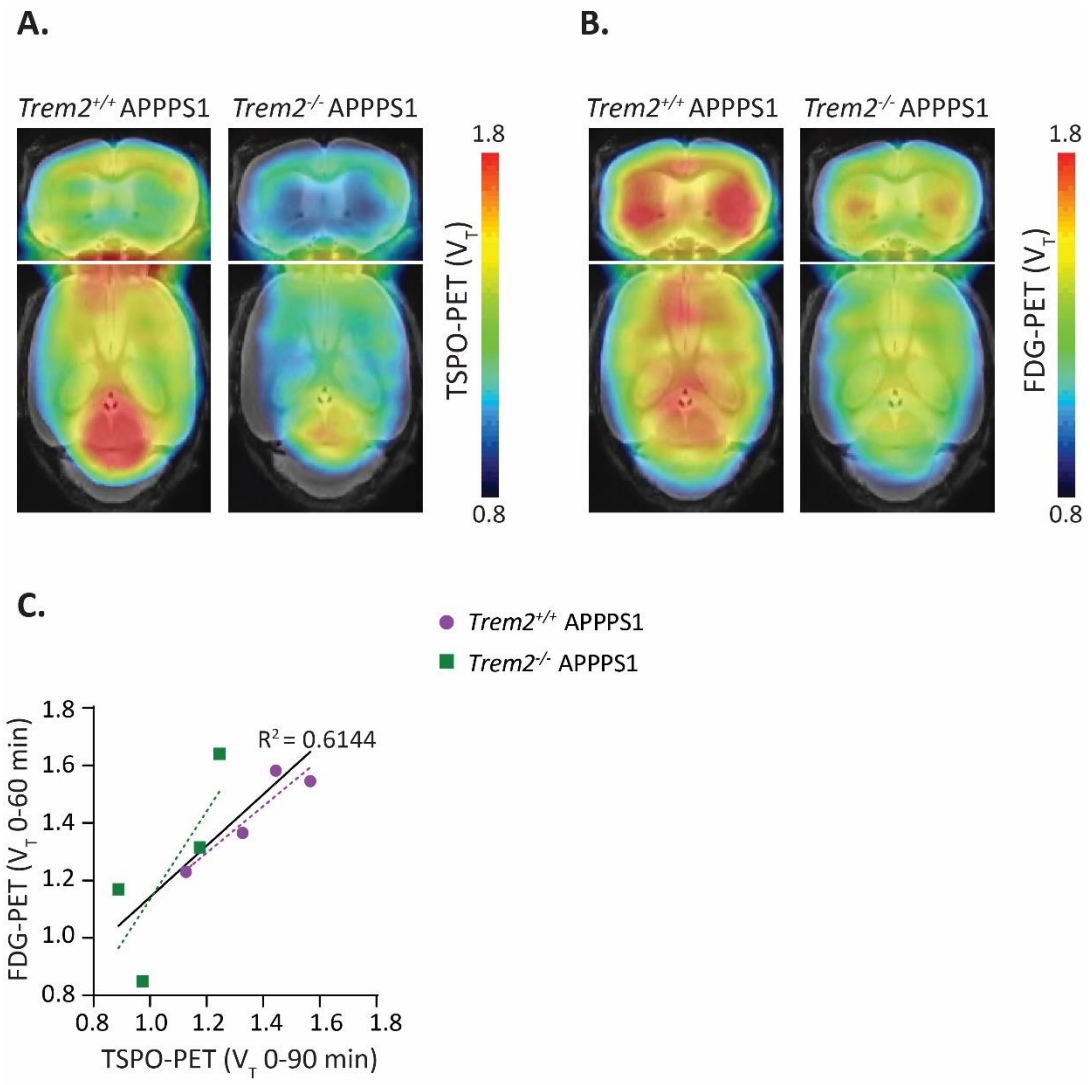

Fig. S3 Dynamic FDG- and TSPO-PET imaging

(A & B). Coronal and axial slices show group averages of TSPO-PET (V_T) (A) and FDG-PET (V_T) (B) of *Trem2*$^{+/+}$ APPPS1 and *Trem2*$^{-/-}$ APPPS1 mice. V_T: volume of distribution.
(C). Positive correlation between glucose uptake (FDG-PET (V_T)) and microglial activation (TSPO-PET (V_T)) deriving from a blood flow adjusted quantification via kinetic modeling of dynamic acquisition with an image derived input function.

Supplementary figure 4

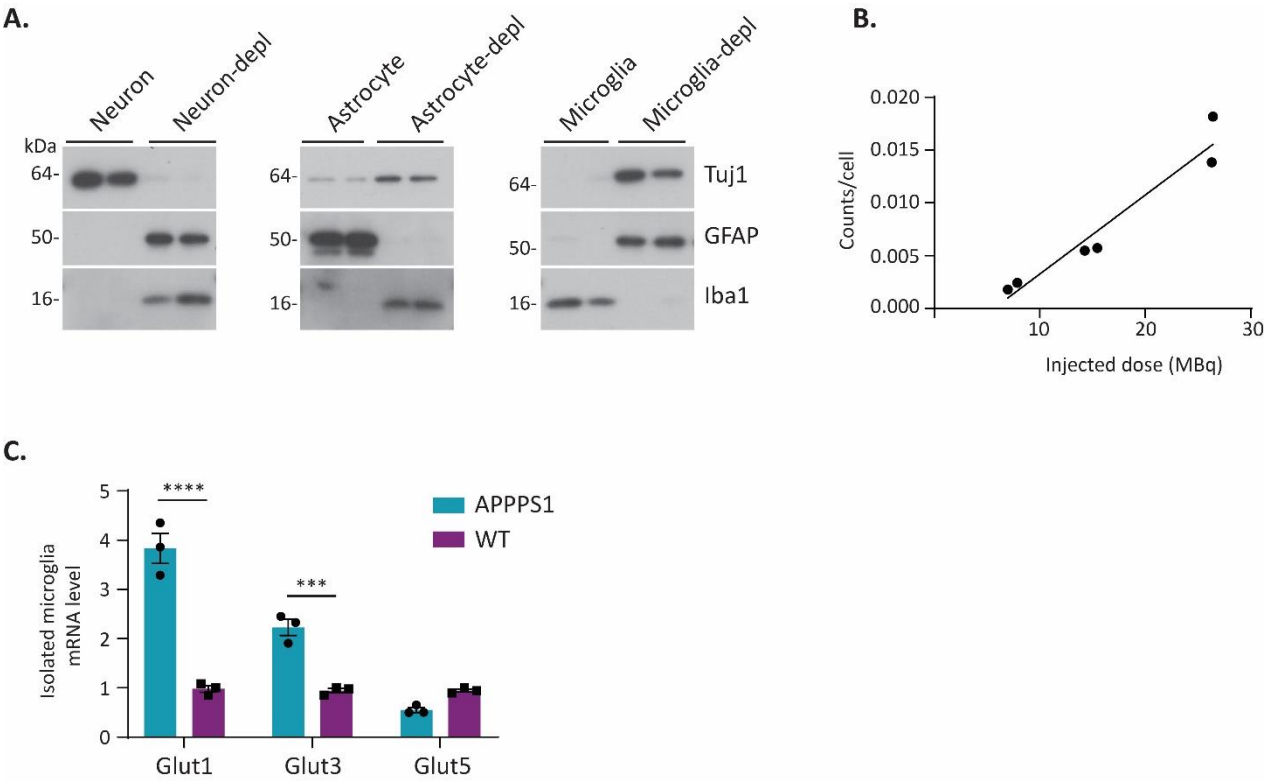

Fig. S4 Quality controls for magnetic-activated cell sorting

(A). The identity of neural cell types was verified by detection of Tuj1 for neurons, GFAP for astrocytes, and Iba1 for microglia.
(B). FDG counts per cell in neuron fraction is increased along with a higher injection dose of FDG.
(C). mRNA level of glucose transporters (Glut1, 3 and 5) in isolated microglia from APPPS1 and WT animals. Mean ± s.e.m. of n = 3. Two-way ANOVA $P < 0.0001$; Bonferroni post hoc tests, Glut5 WT vs. APPPS1 nonsignificant; ***$P < 0.001$; ****$P < 0.0001$.

Supplementary figure 5

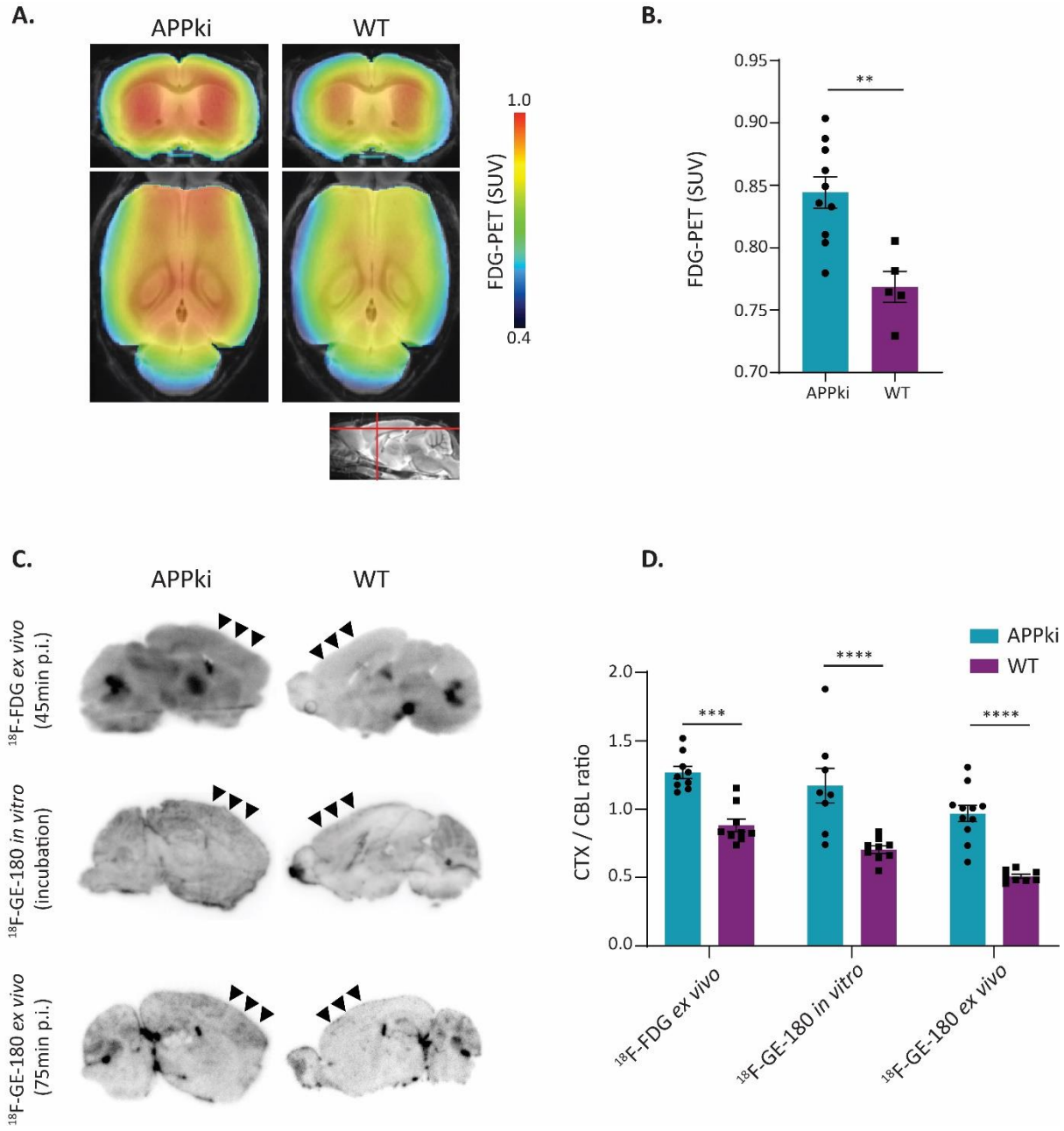

Fig. S5 FDG-PET and autoradiography in *App^{NL-G-F}* animals

(A). Coronal and axial slices show group averages of FDG-PET (SUV) per group of *App^{NL-G-F}* animals (APPki) and WT projected upon a standard MRI T1 atlas.
(B). Quantification of cortical glucose uptake measured by *in vivo* FDG-PET of WT and APPki. Mean ± s.e.m. of n = 5-10. Mann-Whitney test P = 0.0047.
(C). Representative images of *ex vivo* and *in vitro* autoradiography of ^{18}F-FDG and ^{18}F-GE-180 (TSPO).
(D). Quantification of cortex to cerebellum ratios (CTX / CBL ratio) between APPki and WT mice. Mean ± s.e.m. of n = 8-11 analyzed slices. Two-way ANOVA; Bonferroni post hoc tests, ***P < 0.001; ****P < 0.0001.

Supplementary figure 6

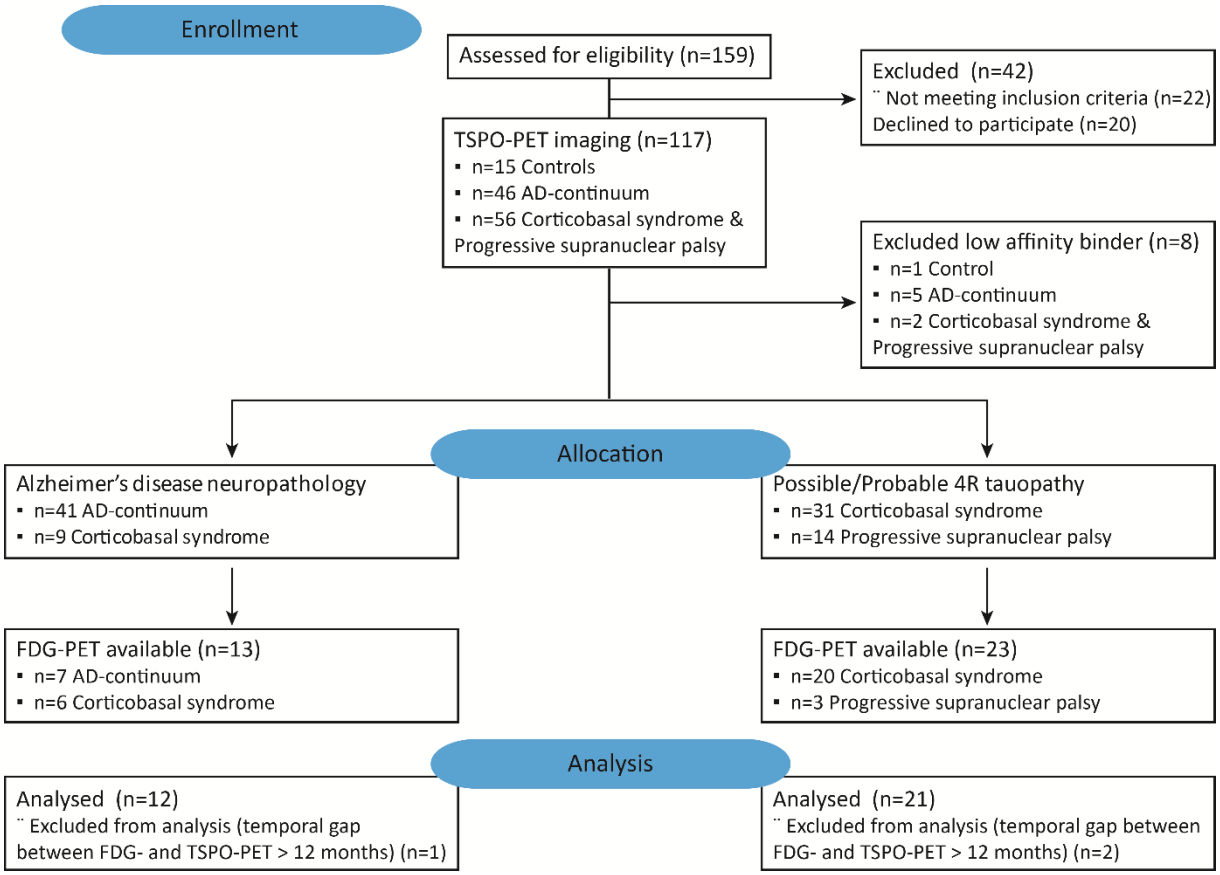

Fig. S6 CONSORT chart of patient selection

CONSORT chart of patient selection. The in-house Activity of Cerebral Networks, Amyloid, and Microglia in Alzheimer's Disease (ActiGliA) cohort is composed of patients with AD, 4-repeat tauopathies, as well as healthy controls who undergo a multimodal imaging paradigm together with fluid biomarkers.

Supplementary figure 7

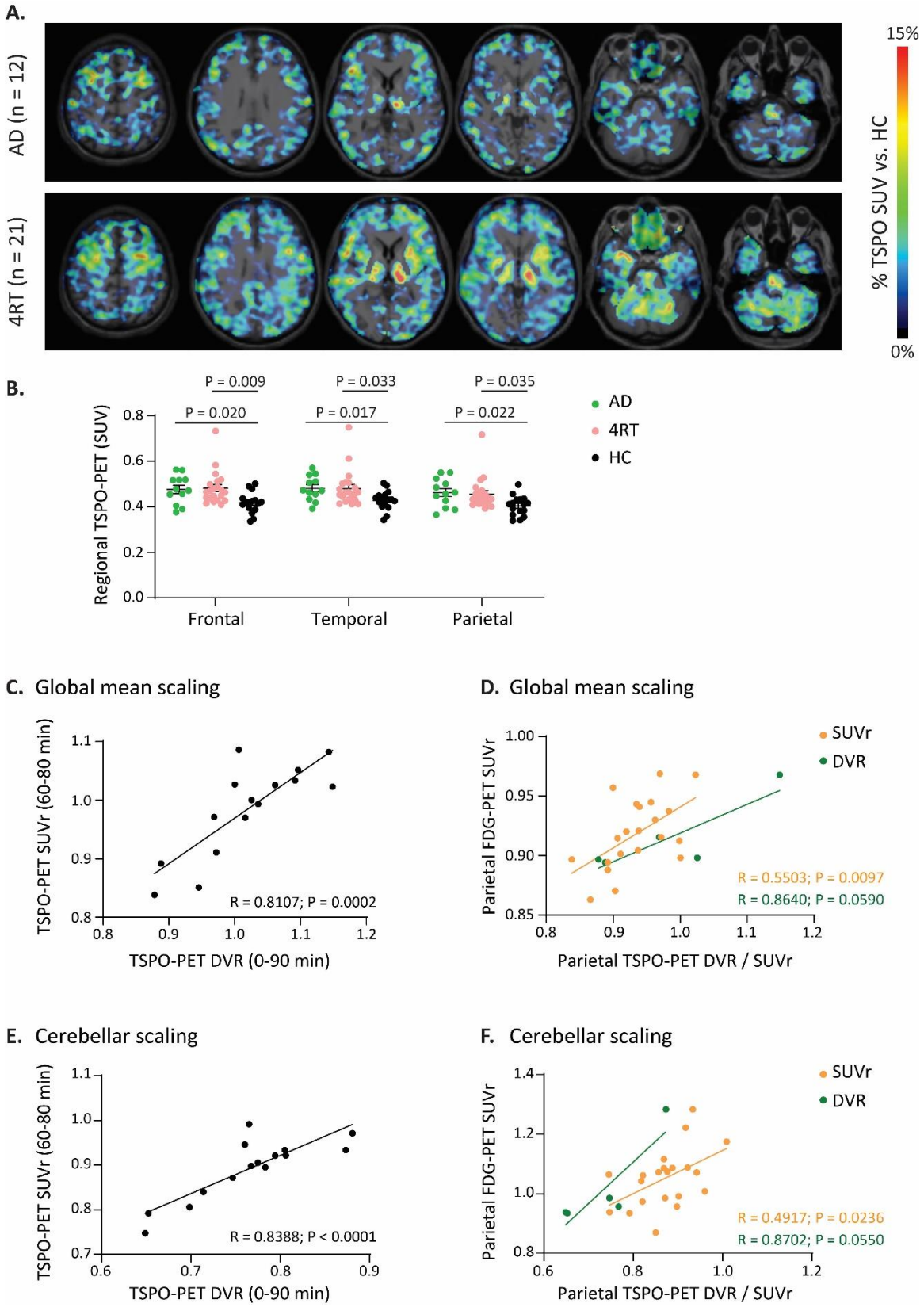

Fig. S7 Regional TSPO- and FDG-PET alterations and associations in patients with Alzheimer's disease and 4-repeat tauopathies

(A). Regional percentage changes of TSPO-PET in patients with Alzheimer's disease (AD, n = 12) or 4-repeat tauopathies (4RT, n = 21) when compared to healthy controls (n = 16).

(B). Quantification of TSPO-PET SUV in patients. Mean ± s.e.m. Two-way ANOVA; Post hoc analysis is controlled for age and sex.
(C & E). Correlation between dynamic TSPO-PET imaging and SUVr quantification of TSPO-PET for pooled frontal, temporal and parietal regions of interest. DVR: distribution volume ratio.
(D & F). Correlation between TSPO-PET DVR (n=5) and SUVr (n=21) with FDG-PET SUVr in the parietal lobe. No adjustment for age and sex was made due to the small n of DVR data.